



HAL
open science

Dynamics of a regularized and bistable Ericksen bar using an extended Lagrangian approach

Stéphane Bourgeois, Nicolas Favrie, Bruno Lombard

► **To cite this version:**

Stéphane Bourgeois, Nicolas Favrie, Bruno Lombard. Dynamics of a regularized and bistable Ericksen bar using an extended Lagrangian approach. 2020. hal-02519362

HAL Id: hal-02519362

<https://hal.science/hal-02519362>

Preprint submitted on 26 Mar 2020

HAL is a multi-disciplinary open access archive for the deposit and dissemination of scientific research documents, whether they are published or not. The documents may come from teaching and research institutions in France or abroad, or from public or private research centers.

L'archive ouverte pluridisciplinaire **HAL**, est destinée au dépôt et à la diffusion de documents scientifiques de niveau recherche, publiés ou non, émanant des établissements d'enseignement et de recherche français ou étrangers, des laboratoires publics ou privés.

Dynamics of a regularized and bistable Ericksen bar using an extended Lagrangian approach

Stéphane Bourgeois^a, Nicolas Favrie^{b,*}, Bruno Lombard^a

^a*Aix-Marseille Univ, CNRS, Centrale Marseille, LMA, Marseille, France*

^b*Aix-Marseille Univ, CNRS, IUSTI, Polytech Marseille, Marseille, France*

Abstract

The motivation of this work is to better understand the dynamic behaviour of bistable structures presenting an analogy with regularized Ericksen bars. The archetype of such structures is the bistable tape spring, which exhibits a particular scenario of deployment, from the stable coiled configuration to the straight stable configuration: at each time of the deployment, the geometry of the tape is similar to a two-phase bar with a coiled part and a straight part separated by a transition zone that moves along the tape. One goal of this work is to show that a regularized and bistable Ericksen bar model contains all the properties to reproduce such a dynamic behaviour. The mathematical structure of this model presents a locally non-convex potential with two minima and a dependence of higher order terms. Some similarities exist between this model and the Euler-Korteweg system with a Van der Waals equation. To study numerically the dynamic behaviour of such models, it is necessary to solve a dispersive and conditionally hyperbolic system. For this purpose, the Lagrangian of the regularized bistable Ericksen model is extended and penalized. Variable boundary conditions are deduced from Hamilton's principle and are used to control the evolution of the system. Dispersion analysis allows to determine the numerical parameters of the model. The obtained non-homogeneous hyperbolic system can be solved by standard splitting strategy and finite-volume methods. Numerical simulations illustrate how the parameters of the model influence the width and the propagation speed of the transition zone. The effect of energy dissipation is also examined. Finally, comparisons with an exact kink wave solution indicate that the extended Lagrangian solution reproduces well the dynamics of the original Lagrangian.

Keywords: nonlinear dynamics, regularized Ericksen bar model, bistability, kink wave, enriched continuum mechanics, extended Lagrangian, hyperbolic systems

1. Introduction

The starting point of this work relies on the dynamic behaviour of bistable tape springs. Such tapes, that exhibit two stable states, can be easily designed with fiber-reinforced composite materials [13]. With this manufacturing technique, one can obtain a straight tape with a curved cross-section that possesses a second stable cylindrical coiled configuration, with flattened cross-section. Starting from a coiled configuration, the deployment can be launched by modifying

*Corresponding author. Tel.: +33 404-91-10-69-56.

Email addresses: `stephane.bourgeois@centrale-marseille.fr` (Stéphane Bourgeois), `nicolas.favrie@univ-amu.fr` (Nicolas Favrie), `lombard@lma.cnrs-mrs.fr` (Bruno Lombard)

the cross-section shape at one end. Figure 1 illustrates the particular kinematics of deployment which is similar to the unrolling of a party whistle. At each time, the tape exhibits an uncoiled straight part and a coiled part, separated by a travelling transition zone.

The modeling of tape springs has been the subject of several works [26, 32, 15] and a rod model with flexible cross-section [14, 23, 24, 22] has been proposed that accounts for the particular deployment kinematics of bistable tape springs [14]. More specifically, a recent work has shown an analogy between the behaviour of a classical (non bistable) tape and the one of a regularized Ericksen bar in statics [22]. This later model leads to a deep understanding of the mechanisms underlying the folding of tape springs: local non-convexity of the strain energy density (of the rod model) leading to the appearance of folds, additional higher order terms that govern the transition zones, boundary conditions prescribed on higher order terms (which are linked to the cross-section shape) that modify the bifurcation diagrams and the location of the folds.

One goal of this article is to see whether a regularized Ericksen bar model can reproduce the dynamic behaviour of bistable tape springs. Dynamics is then introduced in the model and a non-convex strain energy with two minima is considered. In the literature, the dynamics of regularized Ericksen bar models has been widely studied in the framework of phase transformations. This model is also used to account for the formation of spatial patterns that can be observed in some experiments. Nevertheless, most papers are focused on the study of a (non bistable) regularized Ericksen bar on elastic foundation [27, 16, 30, 29]. One originality of our work resides in the study of a *bistable* regularized Ericksen for which the *dynamic effects* are launched by *quasi-static boundary conditions prescribed on higher order terms*.



Figure 1: Dynamic deployment of a bistable tape spring. From a coiled configuration to a deployed straight one, from left to right.

The model proposed in section 2 follows from a *master Lagrangian* formulation and from Hamilton's principle. Qualitative properties are proven, and an exact kink wave solution is proposed. Our model combines two main difficulties:

- The equation of state is locally non convex. The system is then elliptic in a bounded range of states, and hence the solution is not bounded in a finite time if no regularization is considered.
- The regularizing term in the master Lagrangian involves second-order gradient which prevents from using classical numerical methods for hyperbolic systems.

The mathematical structure of this model is similar to that of Euler-Korteweg system with a Van der Waals equation of state (or Navier-Stokes-Korteweg NSK system, if dissipation is

taken into account). Various methods have been developed to solve such systems, see e.g. [11, 2, 20, 5] to deal with liquid-vapor transition and capillary films. As highlighted in [25], “the mixed hyperbolic-elliptic structure of the classical NSK models prevents the use of stabilised discretizations to cover convection dominated flow regimes”. The developed methods need to consider a relaxed model whose numerical cost is important. Indeed, at each time step an elliptic operator [19] or a diffusion equation has to be solved on the whole computational domain.

To circumvent these numerical problems, we use here the so-called *extended Lagrangian* technique developed in [10] for the Serre-Green-Nagdhi equations of shallow water fluid mechanics, and in [4] for the nonlinear Schrödinger equations. For this purpose, we introduce a micro-inertia term and a penalization term (section 3). Hamilton’s principle leads to a family of boundary conditions, allowing to control the shifting from a stable configuration to another one. An energy balance is established. A dispersion analysis shows the link between the original and the extended formulations. The introduction of dissipation in the original model (with a Kelvin-Voigt model) and in the extended model (with a source term) is addressed in section 4.

The resulting EDP system is well suited to numerical simulation. Here it is split into a propagative term and a relaxation term, solved successively by a splitting technique (section 5). The propagative term is solved by a standard finite-volume scheme with flux limiters, while the relaxation term is solved exactly. Theoretical and numerical considerations allow to choose the parameters of the extended Lagrangian.

Numerical experiments illustrate the influence of the parameters of the extended Lagrangian (section 6). Various dynamics are obtained, combining dispersion and nonlinearity. The generation of a kink wave by a variable boundary condition is observed, in accordance with real experiments on tapes. This kink wave is successfully compared with the exact travelling wave obtained in section 2, which indicates that the extended Lagrangian captures well the dynamics of the original master Lagrangian. A parametric study of this kink wave is carried out as a function of the physical parameters. Finally, a conclusion and perspectives are drawn (section 7).

2. Original regularised Ericksen model

2.1. Hamilton’s principle

We propose a 1D model derived from a bistable Ericksen model [22]. The evolution equations as well as the boundary conditions follow from Hamilton’s principle.

Lagrangian. We note u the displacement, $v = \partial_t u$ the velocity, $\varepsilon = \partial_x u$ the strain, and $\partial_x \varepsilon$ the strain gradient. The kinetic energy \mathcal{T} and the internal energy \mathcal{V} are:

$$\mathcal{T} = \frac{\rho}{2} (\partial_t u)^2, \quad \mathcal{V} = W(\varepsilon) + \frac{\alpha}{2} (\partial_x \varepsilon)^2, \quad (1)$$

where ρ (kg.m^{-3}) is the density, W ($\text{kg.m}^{-1}.\text{s}^{-2}$) is the strain energy associated to the Ericksen bar model, and α (kg.m.s^{-2}) introduces a dependence of the energy on the strain gradient. The Ericksen bistable model corresponds to the following assumptions about W :

- W is C^2 ,
- $W'' = \frac{\partial^2 W}{\partial \varepsilon^2}$ vanishes at ε_1 and ε_2 , where $0 < \varepsilon_1 < \varepsilon_2$,
- $W'' < 0$ on $]\varepsilon_1, \varepsilon_2[$, $W'' \geq 0$ outside this interval,

- $W'(\varepsilon_1) > 0$ and $W'(\varepsilon_2) < 0$, where $W' = \frac{\partial W}{\partial \varepsilon}$.

An example of energy satisfying these assumptions is the polynomial of degree 4:

$$W(\varepsilon) = a_2 \varepsilon^2 + a_3 \varepsilon^3 + a_4 \varepsilon^4, \quad (2)$$

where $a_2 = 59/24$, $a_3 = -7/6$ and $a_4 = 7/48$. The energy W is then non-convex on $]\varepsilon_1, \varepsilon_2[$, with $\varepsilon_{1,2} = 2 \mp \frac{5}{\sqrt{21}}$. The three equilibrium points where W' vanishes are 0, $\varepsilon_1^0 = 3 - \frac{2}{\sqrt{7}}$ and $\varepsilon_2^0 = 3 + \frac{2}{\sqrt{7}} > \varepsilon_2$. The stable equilibrium points where $W'' > 0$ are 0 and ε_2^0 . In the following, we will focus on the only non-zero stable equilibrium point ε_2^0 . These points are summarized in the table 1. Figure 2 represents W and its derivatives. The horizontal scale differs between (a) and (b)-(c) to better illustrate the double well of W .

	0	$\varepsilon_1 = 2 - \frac{5}{\sqrt{21}}$	$\varepsilon_1^0 = 3 - \frac{2}{\sqrt{7}}$	$\varepsilon_2 = 2 + \frac{5}{\sqrt{21}}$	$\varepsilon_2^0 = 3 + \frac{2}{\sqrt{7}}$
W'	0	+	0	-	0
W''	+	0	-	0	+

Table 1: Particular points of double-well energy (2).

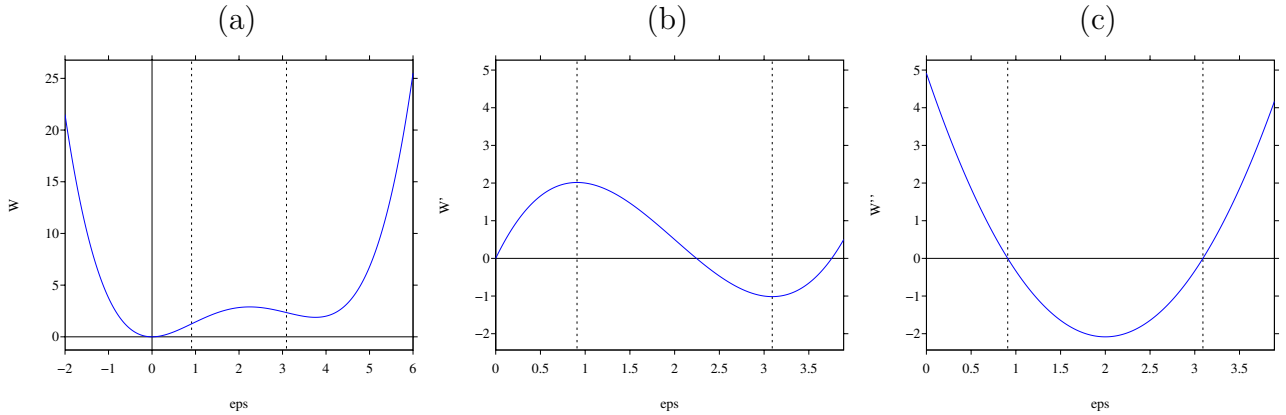


Figure 2: (a): W , (b): W' , (c): W'' . The dotted vertical lines represent the bounds of the interval $]\varepsilon_1, \varepsilon_2[$ within which the energy W (2) is not convex.

The spatial domain is $[0, L]$. The action of the master Lagrangian $\mathcal{L} = \mathcal{T} - \mathcal{V}$ is stationary, which yields the Euler-Lagrange equations and the boundary conditions. We successively detail the equations so-obtained.

Evolution equations. Euler-Lagrange's equations lead to the system

$$\begin{cases} \partial_t \varepsilon - \partial_x v = 0, & (3a) \\ \rho \partial_t v - \partial_x \sigma = 0. & (3b) \end{cases}$$

In (3b), σ is the total stress in the bar:

$$\sigma(\varepsilon, \partial_{xx}^2 \varepsilon) = W'(\varepsilon) - \alpha \partial_{xx}^2 \varepsilon. \quad (4)$$

For smooth solutions, the system (3) admits the additional conservation law

$$\partial_t E - \partial_x \Pi = 0, \quad (5)$$

where $E = \mathcal{T} + \mathcal{V}$ is the density of energy and Π is the Poynting vector (here a scalar):

$$E = \frac{\rho}{2} v^2 + W(\varepsilon) + \frac{\alpha}{2} (\partial_x \varepsilon)^2, \quad \Pi = v \sigma + \alpha \partial_t \varepsilon \partial_x \varepsilon. \quad (6)$$

In Π , the term $\alpha \partial_t \varepsilon \partial_x \varepsilon$ is an *interstitial work* [4]. By noting \mathcal{E} the total energy and \mathcal{P} the power of the efforts

$$\mathcal{E} = \int_0^L E dx, \quad \mathcal{P} = [\Pi]_0^L, \quad (7)$$

integration of (6) along the bar yields

$$\frac{d}{dt} \mathcal{E} = \mathcal{P}. \quad (8)$$

Initial conditions. The master system (3) is completed by the initial conditions

$$\varepsilon(x, 0) = \varepsilon_0(x), \quad v(x, 0) = v_0(x), \quad x \in [0, L]. \quad (9)$$

The second stable equilibrium state is obtained by choosing

$$\varepsilon_0(x) = \varepsilon_2^0, \quad v_0(x) = 0. \quad (10)$$

Boundary conditions. On the edges of the domain, stationarity of the action yields

- $u(0, t) = f_u(t)$ and $\partial_x \varepsilon(0, t) = 0$,
- $\varepsilon(L, t) = f_\varepsilon(t)$ and $\sigma(L, t) = 0$,

where f_u and f_ε are arbitrary functions. The displacement not being a variable of (3), the boundary condition on u is differentiated with respect to time, and we note $f_v = (f_u)'$. One finally obtains the 4 boundary conditions:

$$\begin{cases} v(0, t) = f_v(t), & (11a) \\ \partial_x \varepsilon(0, t) = 0, & (11b) \\ \varepsilon(L, t) = f_\varepsilon(t), & (11c) \\ \sigma(L, t) = 0. & (11d) \end{cases}$$

Based on the conditions (11), the power (7) is

$$\mathcal{P} = -(f_u(t))' \sigma(0, t) + \alpha (f_\varepsilon(t))' \partial_x \varepsilon(L, t). \quad (12)$$

If the imposed displacements f_u and strain f_ε are constant, then the power of the forces is zero and the total energy is conserved (8).

2.2. System of PDE

Setting

$$\mathbf{U} = \begin{pmatrix} \varepsilon \\ v \end{pmatrix}, \quad \mathbf{f}(\mathbf{U}) = \begin{pmatrix} -v \\ -\frac{1}{\rho} W'(\varepsilon) \end{pmatrix}, \quad \mathbf{S} = \begin{pmatrix} 0 & 0 \\ -\alpha & 0 \end{pmatrix}, \quad (13)$$

the equations (3) lead to the dispersive system

$$\partial_t \mathbf{U} + \partial_x \mathbf{f}(\mathbf{U}) = \mathbf{S} \partial_{xxx}^3 \mathbf{U}, \quad (14)$$

with the Jacobian matrix

$$\mathbf{A}(\mathbf{U}) = \begin{pmatrix} 0 & -1 \\ -\frac{W''(\varepsilon)}{\rho} & 0 \end{pmatrix}. \quad (15)$$

The eigenvalues of \mathbf{A} are

$$\Lambda^{(1,2)} = \pm \sqrt{\frac{W''(\varepsilon)}{\rho}}. \quad (16)$$

On $]\varepsilon_1, \varepsilon_2[$, $W''(\varepsilon) < 0$, thus the eigenvalues $\Lambda^{(1,2)}$ are complex. At ε_1 and ε_2 , $\Lambda^{(1)} = \Lambda^{(2)} = 0$ and the Jacobian \mathbf{A} is not diagonalizable. The PDE (14) is thus not hyperbolic on $[\varepsilon_1, \varepsilon_2]$.

2.3. Dispersion analysis

The equations (3) are linearized around a uniform state $(\bar{\varepsilon}, \bar{v})$. We inject $\varepsilon = \bar{\varepsilon} + \zeta \tilde{\varepsilon}$ and $v = \bar{v} + \zeta \tilde{v}$ into (3), with $0 < \zeta \ll 1$, and we write for simplicity $W'' = W''(\bar{\varepsilon})$. At the order 1 in ζ , one obtains

$$\begin{cases} \partial_t \tilde{\varepsilon} - \partial_x \tilde{v} = 0, & (17a) \\ \rho \partial_t \tilde{v} - \partial_x (W'' \tilde{\varepsilon}) = -\alpha \partial_{xxx}^3 \tilde{\varepsilon}. & (17b) \end{cases}$$

Perturbations are written as harmonic plane waves: $\tilde{\varepsilon} = \hat{\varepsilon} e^{i(\omega t - kx)}$ and $\tilde{v} = \hat{v} e^{i(\omega t - kx)}$, where ω is the angular frequency and k is the wavenumber. It yields the system

$$\underbrace{\begin{pmatrix} \omega & k \\ k(W'' + \alpha k^2) & \omega \rho \end{pmatrix}}_{\mathbf{M}} \begin{pmatrix} \hat{\varepsilon} \\ \hat{v} \end{pmatrix} = \mathbf{0}. \quad (18)$$

To get solutions other than the null trivial solution, one must satisfy $\det(\mathbf{M}) = 0$, which leads to the dispersion relation

$$\omega(k) = k \sqrt{\frac{W'' + \alpha k^2}{\rho}}, \quad (19)$$

and hence to the phase velocity

$$c_p(k) = \frac{\omega(k)}{k} = \sqrt{\frac{W'' + \alpha k^2}{\rho}}. \quad (20)$$

Phase velocity is real if $k^2 > -W''/\alpha$. Outside $]\varepsilon_1, \varepsilon_2[$, the energy is convex and waves propagate at all wavelengths. On the non-convexity interval $]\varepsilon_1, \varepsilon_2[$, $W'' < 0$ and waves propagate above the critical wavelength k_c :

$$k > k_c = \sqrt{-W''/\alpha}, \quad (21)$$

i.e. for sufficiently short wavelengths. If $k < k_c$, then ω is purely imaginary and $\tilde{\varepsilon} = \hat{\varepsilon} e^{|\omega|t} e^{-ikx}$. The solution ε then grows unbounded and in finite time comes out of $]\varepsilon_1, \varepsilon_2[$, which stabilizes the system. For large k , the phase velocity tends asymptotically to the line $\sqrt{\alpha/\rho} k$. From now on, we will designate by *master wave* the solution of phase velocity c_p . The dispersion properties are illustrated in figure 3, for three strain values: $\bar{\varepsilon} = 0$ i.e. $W'' > 0$ (a), $\bar{\varepsilon} = \varepsilon_1$ i.e. $W'' = 0$ (b), $\bar{\varepsilon} = (\varepsilon_1 + \varepsilon_2)/2$ i.e. $W'' < 0$ (c).

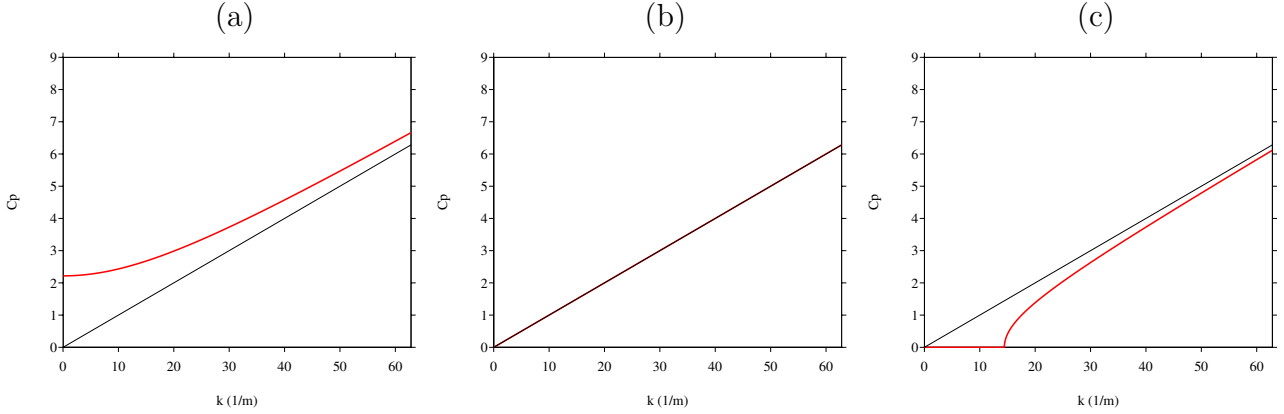


Figure 3: Master Lagrangian phase velocity (20), for three values of $\bar{\varepsilon}$, leading to: $W'' > 0$ (a), $W'' = 0$ (b), and $W'' < 0$ (c). The line through the origin is the asymptote $\sqrt{\alpha/\rho} k$.

2.4. Kink wave solution

Two observables characterize the unfolding of a bistable tape spring: the speed of propagation of the front V and the thickness of the transition zone D . The goal of this section is to check the possibility to observe a kink wave for a bistable regularized Ericksen bar, that can mimic the scenario of switching from a stable configuration to another one. By dimensional analysis of (3), one obtains

$$V \propto \sqrt{\frac{a_i}{\rho}}, \quad D \propto \sqrt{\frac{\alpha}{a_i}}. \quad (22)$$

The goal of this section is to go further and to give explicit expressions of these quantities. To do so, we introduce the change of variable $\xi = x - Vt$. Injecting ξ into (3) provides

$$\rho V^2 \varepsilon - W'(\varepsilon) + \alpha \partial_{\xi\xi}^2 \varepsilon = C_2, \quad (23)$$

where C_2 is an integration constant to be determined. Integration yields

$$\begin{aligned} \frac{\alpha}{2} \left(\frac{d\varepsilon}{d\xi} \right)^2 &= a_4 \varepsilon^4 + a_3 \varepsilon^3 + \left(a_2 - \rho \frac{V^2}{2} \right) \varepsilon^2 + C_2 \varepsilon + C_3, \\ &\equiv \varphi(\varepsilon) \geq 0, \end{aligned} \quad (24)$$

where C_3 is an integration constant to be determined. For a kink, the support of the travelling wave is bounded; on an interval $[\varepsilon_A, \varepsilon_B]$, φ is a fourth-degree polynomial. Outside this interval, we must have $\frac{d\varepsilon}{d\xi} = 0$, and hence (24) leads to $C_3 = 0$. The unique possible choice is

$$\varphi(\varepsilon) = \begin{cases} F(\varepsilon - \varepsilon_A)^2(\varepsilon - \varepsilon_B)^2 & \text{on } [\varepsilon_A, \varepsilon_B], \\ 0 & \text{outside.} \end{cases} \quad (25)$$

After identifying (24) and (25) on the interval $[\varepsilon_A, \varepsilon_B]$, we get $F = a_4$, $C_2 = 0$, and

$$\varepsilon_A = 0, \quad \varepsilon_B = -\frac{a_3}{2a_4}, \quad V = \sqrt{\frac{2}{\rho} \left(a_2 - \frac{a_3^2}{4a_4} \right)}, \quad (26)$$

which specifies (22). The constant state ε_B and the velocity V do not depend on the regularization parameter α . Since $\varepsilon_A < \varepsilon_B$, the solution is a *kink wave* [3].

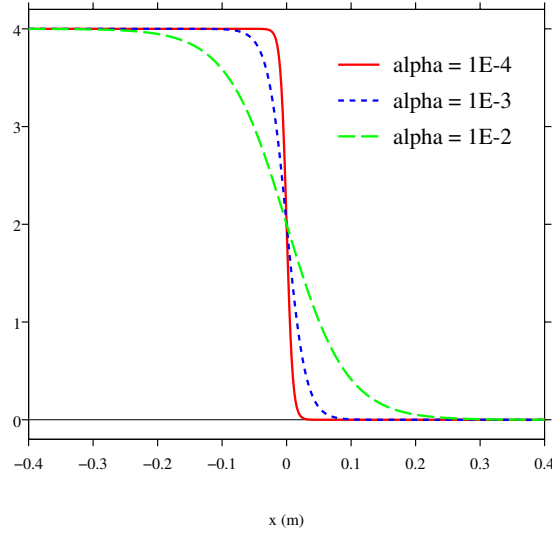


Figure 4: Influence of the regularization parameter α on the shape of the kink wave.

Integration of (24) yields the profile of ε :

$$\varepsilon(\xi) = \frac{\varepsilon_B}{1 + \exp\left(\varepsilon_B \sqrt{\frac{2a_4}{\alpha}} \xi\right)}. \quad (27)$$

Contrary to the propagation speed of the front, the profile of the kink wave depends on α . Figure 4 illustrates the evolution of ε in terms of α . When $\alpha \rightarrow 0$, then ε tends towards a Heaviside profile. Based on (27), one computes ξ_N such that $\varepsilon(\xi_N) = N/100 \varepsilon_B$:

$$\xi_N = \frac{1}{\varepsilon_B} \ln\left(\frac{100}{N} - 1\right) \sqrt{\frac{\alpha}{2a_4}}. \quad (28)$$

Defining the width of the kink as $D = 2\xi_N$, then $D \propto \sqrt{\alpha/a_4}$. Once again, it specifies (22).

3. Extended Lagrangian formulation

3.1. Hamilton's principle

Here, the motion equations as well as the boundary conditions are derived from the Hamilton's principle applied on an extended Lagrangian.

Lagrangian. We introduce the dimensionless variable η and we define the extended Lagrangian $\mathcal{L}_e = \mathcal{T}_e - \mathcal{V}_e$, with

$$\mathcal{T}_e = \frac{\rho}{2} (\partial_t u)^2 + \frac{\beta}{2} (\partial_t \eta)^2, \quad \mathcal{V}_e = W(\varepsilon) + \frac{\alpha}{2} (\partial_x \eta)^2 + \frac{\lambda}{2} (\varepsilon - \eta)^2, \quad (29)$$

where $\beta \geq 0$ (kg.m⁻¹) governs the micro-inertia and $\lambda \geq 0$ (kg.m⁻¹.s⁻²) is a penalization parameter. We expect $\eta = \varepsilon + \mathcal{O}(\lambda^{-1})$, so as the extended Lagrangian $\mathcal{T}_e - \mathcal{V}_e$ recovers the master Lagrangian $\mathcal{T} - \mathcal{V}$ when $\lambda \rightarrow +\infty$ and $\beta \rightarrow 0$.

The micro-inertia term is required to get an evolution equation for η . Physically, it evokes the Poisson effect in the Rayleigh-Lamb equation on a thin plate. In the present case, the effect is considered as small and is linear.

The stationarity of the extended Lagrangian yields the Euler-Lagrange equations and the boundary conditions. The equations so-obtained are detailed successively.

Evolution equations. We define $w = \partial_t \eta$ and $p = \partial_x \eta$. Euler-Lagrange's equations lead to the extended system

$$\begin{cases} \partial_t \varepsilon - \partial_x v = 0, & (30a) \\ \rho \partial_t v - \partial_x \sigma_e = 0, & (30b) \\ \partial_t \eta = w, & (30c) \\ \partial_t p - \partial_x w = 0, & (30d) \\ \beta \partial_t w - \partial_x (\alpha p) = \lambda (\varepsilon - \eta). & (30e) \end{cases}$$

In (30b), σ_e is the total stress in the bar:

$$\begin{aligned} \sigma_e(\varepsilon, \eta) &= W'(\varepsilon) + \lambda(\varepsilon - \eta), \\ &= s(\varepsilon) - \lambda \eta, \end{aligned} \quad (31)$$

where

$$\begin{aligned} s(\varepsilon) &= W'(\varepsilon) + \lambda \varepsilon, \\ &\equiv (2 a_2 + \lambda) \varepsilon + 3 a_3 \varepsilon^2 + 4 a_4 \varepsilon^3. \end{aligned} \quad (32)$$

Injecting (30e) into (30b), one obtains

$$\rho \partial_t v - \partial_x \left(W'(\varepsilon) - \alpha \partial_{xx}^2 \eta \right) = \beta \partial_{xtt}^3 \eta. \quad (33)$$

Assuming $\eta = \varepsilon + \mathcal{O}(\lambda^{-1})$, then the extended system recovers the master system (3) when $\lambda \rightarrow +\infty$ and $\beta \rightarrow 0$. For smooth solutions, the extended system (30) admits the additional conservation law

$$\partial_t E_e - \partial_x \Pi_e = 0, \quad (34)$$

where $E_e = \mathcal{T}_e + \mathcal{V}_e$ is the density of energy

$$E_e = \frac{\rho}{2} v^2 + \frac{\beta}{2} w^2 + W(\varepsilon) + \frac{\alpha}{2} p^2 + \frac{\lambda}{2} (\varepsilon - \eta)^2, \quad (35)$$

and Π_e is the Poynting vector (here a scalar)

$$\begin{aligned} \Pi_e &= v(W' + \lambda(\varepsilon - \eta)) + \alpha p w, \\ &= v \sigma_e + \alpha p w. \end{aligned} \quad (36)$$

By noting \mathcal{E}_e the total energy and \mathcal{P}_e the power of the internal efforts

$$\mathcal{E}_e = \int_0^L E_e dx, \quad \mathcal{P}_e = [\Pi_e]_0^L, \quad (37)$$

integration of (35) along the bar yields

$$\frac{d}{dt} \mathcal{E}_e = \mathcal{P}_e. \quad (38)$$

Initial conditions. The extended system (30) is completed by the initial conditions

$$\varepsilon(x, 0) = \varepsilon_0(x), \quad v(x, 0) = v_0(x), \quad \eta(x, 0) = \eta_0(x), \quad p(x, 0) = p_0(x), \quad w(x, 0) = w_0(x), \quad (39)$$

where $x \in [0, L]$. In the numerical experiments of section 6.2, a bar at equilibrium is submitted to variable boundary conditions. For this purpose, we consider the second stable equilibrium state ε_2^0 . We deduce η_0 from $\sigma_e(\varepsilon_0, \eta_0) = 0$ (31) and from $W'(\varepsilon_2^0) = 0$ (32). All other fields are zero. Hence the initial conditions are

$$\varepsilon(x, 0) = \varepsilon_2^0, \quad v(x, 0) = 0, \quad \eta(x, 0) = \varepsilon_2^0, \quad p(x, 0) = 0, \quad w(x, 0) = 0, \quad x \in [0, L]. \quad (40)$$

Boundary conditions. On the edges of the domain, stationarity of action yields

- $u(0, t) = f_u(t)$ and $p(0, t) = 0$,
- $\eta(L, t) = f_\eta(t)$ and $\sigma_e(L, t) = 0$,

where f_u and f_η are arbitrary functions. Of the four boundary conditions, two involve u and σ_e , which are not variables of (30). To eliminate the displacement, the boundary condition on u is differentiated with respect to time, and one introduces $f_v = (f_u)'$. To eliminate the stress, $\sigma_e(L, t) = 0$ in (31) and $\eta(L, t) = f_\eta(t)$ lead to

$$s(\varepsilon(L, t)) = \lambda f_\eta(t). \quad (41)$$

The relation (41) can be inverted iff s' has a constant sign for all ε . Given W in (2), $s' > 0$ iff

$$\lambda > \lambda_{\min} = \left| \min_{\varepsilon \in \mathbb{R}} W''(\varepsilon) \right| \equiv \frac{25}{12}. \quad (42)$$

As seen in the next section, the condition (42) is necessary and sufficient for the system (30) to be hyperbolic. Under this condition, the boundary condition on $\varepsilon(L, t)$ is

$$\begin{aligned} \varepsilon(L, t) &= s^{-1}(\lambda f_\eta(t)), \\ &\equiv f_\varepsilon(t). \end{aligned} \quad (43)$$

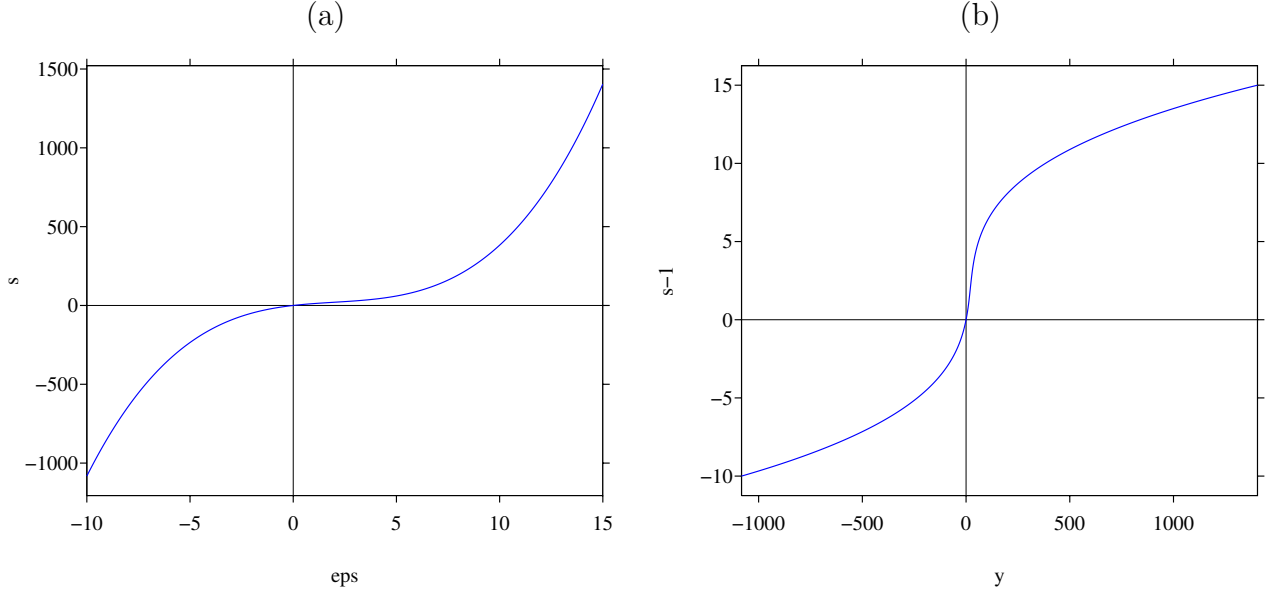


Figure 5: graphs of s (a) and s^{-1} (b), obtained for $\lambda = 10 > \lambda_{\min}$ in (32) and (42).

The graphs of s and s^{-1} are shown in figure 5. Lastly, w and $\partial_t \eta$ are linked by (30c), which provides an additional boundary condition at $x = L$. We finally obtain five boundary conditions on the variables of (30):

$$\begin{cases} v(0, t) = f_v(t), & (44a) \\ p(0, t) = 0, & (44b) \\ \eta(L, t) = f_\eta(t), & (44c) \\ \varepsilon(L, t) = s^{-1}(\lambda f_\eta(t)) \equiv f_\varepsilon(t), & (44d) \\ w(L, t) = (f_\eta)'(t) \equiv f_w(t). & (44e) \end{cases}$$

Based on the conditions (44), the power (37) is

$$\mathcal{P} = -(f_u(t))' \sigma_e(0, t) + \alpha (f_\eta(t))' p(L, t). \quad (45)$$

If the imposed displacements f_u and strain f_η are constant, then the power of the forces is zero and the energy is conserved.

3.2. System of PDE

One defines the characteristic angular frequency

$$\omega_0 = \sqrt{\frac{\lambda}{\beta}}. \quad (46)$$

Setting

$$\mathbf{U}_e = (\varepsilon, v, \eta, p, w)^\top, \quad \mathbf{f}_e(\mathbf{U}_e) = \left(-v, -\frac{1}{\rho} \sigma_e(\varepsilon, \eta), 0, -w, -\frac{\alpha}{\beta} p \right)^\top \quad (47)$$

and

$$\mathbf{S}_e = \begin{pmatrix} 0 & 0 & 0 & 0 & 0 \\ 0 & 0 & 0 & 0 & 0 \\ 0 & 0 & 0 & 0 & 1 \\ 0 & 0 & 0 & 0 & 0 \\ \omega_0^2 & 0 & -\omega_0^2 & 0 & 0 \end{pmatrix}, \quad (48)$$

the system (30) writes

$$\partial_t \mathbf{U}_e + \partial_x \mathbf{f}_e(\mathbf{U}_e) = \mathbf{S}_e \mathbf{U}_e. \quad (49)$$

The eigenvalues of \mathbf{S}_e are 0 (multiplicity 3) and $\pm i\omega_0$. The spectral radius of \mathbf{S}_e is:

$$\varrho(\mathbf{S}_e) = \omega_0. \quad (50)$$

The Jacobian matrix $\mathbf{A}_e = \mathbf{f}'_e(\mathbf{U}_e)$ writes

$$\mathbf{A}_e(\mathbf{U}_e) = \begin{pmatrix} 0 & -1 & 0 & 0 & 0 \\ -\frac{W''(\varepsilon) + \lambda}{\rho} & 0 & \frac{\lambda}{\rho} & 0 & 0 \\ 0 & 0 & 0 & 0 & 0 \\ 0 & 0 & 0 & 0 & -1 \\ 0 & 0 & 0 & -\frac{\alpha}{\beta} & 0 \end{pmatrix}. \quad (51)$$

and has the eigenvalues

$$\Lambda_e^{(1)} = 0, \quad \Lambda_e^{(2,3)} = \pm \sqrt{\frac{W''(\varepsilon) + \lambda}{\rho}}, \quad \Lambda_e^{(4,5)} = \pm \sqrt{\frac{\alpha}{\beta}}. \quad (52)$$

On $[\varepsilon_1, \varepsilon_2]$, $W''(\varepsilon) \geq W''_{\min} = -25/12$. It suffices to choose $\lambda > \lambda_{\min} = 25/12$ to ensure that the system (30) is unconditionnaly hyperbolic. The matrix of right eigenvectors $\mathbf{R}_e = (\mathbf{r}_e^1 | \dots | \mathbf{r}_e^5)$ writes

$$\mathbf{R}_e = \begin{pmatrix} 1 & 1 & 1 & 0 & 0 \\ 0 & -\sqrt{\frac{W''(\varepsilon) + \lambda}{\rho}} & +\sqrt{\frac{W''(\varepsilon) + \lambda}{\rho}} & 0 & 0 \\ \frac{W''(\varepsilon) + \lambda}{\lambda} & 0 & 0 & 0 & 0 \\ 0 & 0 & 0 & 1 & 1 \\ 0 & 0 & 0 & -\sqrt{\frac{\alpha}{\beta}} & +\sqrt{\frac{\alpha}{\beta}} \end{pmatrix}. \quad (53)$$

Its inverse $(\mathbf{R}_e)^{-1}$, which is used in the finite-volume scheme (section 5.2), is

$$(\mathbf{R}_e)^{-1} = \frac{1}{2} \begin{pmatrix} 0 & 0 & \frac{2\lambda}{W''(\varepsilon) + \lambda} & 0 & 0 \\ 1 & -\sqrt{\frac{\rho}{W''(\varepsilon) + \lambda}} & -\frac{\lambda}{W''(\varepsilon) + \lambda} & 0 & 0 \\ 1 & +\sqrt{\frac{\rho}{W''(\varepsilon) + \lambda}} & -\frac{\lambda}{W''(\varepsilon) + \lambda} & 0 & 0 \\ 0 & 0 & 0 & 1 & -\sqrt{\frac{\beta}{\alpha}} \\ 0 & 0 & 0 & 1 & +\sqrt{\frac{\beta}{\alpha}} \end{pmatrix}. \quad (54)$$

In the zone of convexity, a symmetrizer of (49) can be built [9]. The symmetric matrix

$$\mathbf{M}_e(\mathbf{U}_e) = \begin{pmatrix} W''(\varepsilon) + \lambda & 0 & -\lambda & 0 & 0 \\ 0 & \rho & 0 & 0 & 0 \\ -\lambda & 0 & \lambda & 0 & 0 \\ 0 & 0 & 0 & \alpha & 0 \\ 0 & 0 & 0 & 0 & \beta \end{pmatrix}, \quad (55)$$

is appropriate: it ensures that $\mathbf{M}_e \mathbf{A}_e$ is symmetric and that $\mathbf{M}_e \mathbf{S}_e$ is skew-symmetric. Moreover, \mathbf{M}_e is definite-positive iff $W'' > 0$:

$$\mathbf{U}_e^\top \mathbf{M}_e \mathbf{U}_e = W''(\varepsilon) \varepsilon^2 + \rho v^2 + \alpha p^2 + \beta w^2 + \lambda(\varepsilon - \eta)^2. \quad (56)$$

On the contrary, if $W'' < 0$ then \mathbf{M}_e has a negative eigenvalue and no symmetrizer can be built. It is consistent with the fact that the system (49) has a symmetrizer iff there exists a strictly convex energy (see e.g. Theorem 3-2 of [12]).

3.3. Dispersion analysis

We follow the same approach as in section 2.3: linearization, harmonic solution, and cancellation of a determinant. We then obtain the dispersion relation satisfied by $\Omega = \omega^2$:

$$A_4 \Omega^2 + A_2 \Omega + A_0 = 0, \quad (57)$$

where

$$\begin{aligned} A_4 &= \beta \rho > 0, \\ A_2 &= - \left[\left(\beta(W'' + \lambda) + \alpha \rho \right) k^2 + \lambda \rho \right] < 0, \\ A_0 &= \alpha (W'' + \lambda) k^2 \left(k^2 + \frac{W'' \lambda}{\alpha (W'' + \lambda)} \right). \end{aligned} \quad (58)$$

The discriminant of (57) is always positive:

$$\Delta = \left[\left(\beta(W'' + \lambda) - \alpha \rho \right) k^2 - \lambda \rho \right]^2 + 4 \beta \rho \lambda^2 k^2 > 0, \quad (59)$$

so that there are always two real solutions $\Omega^\pm = (\omega^\pm)^2$, with $\Omega^+ > \Omega^-$: the waves associated with Ω^+ and Ω^- are referred to as *fast wave* and *slow wave*, respectively. The sign of A_0 varies: defining the critical wavenumber

$$k_c^e = \sqrt{-\frac{W''\lambda}{\alpha(W'' + \lambda)}}, \quad (60)$$

we get

$$A_0 \begin{cases} > 0 \text{ if } W'' \geq 0 \text{ or if } (W'' < 0 \text{ and } k > k_c^e) & \text{(case 1),} \\ < 0 \text{ else} & \text{(case 2).} \end{cases} \quad (61)$$

The property $\Omega^+ + \Omega^- = -A_2/A_4 > 0$ implies that at least one of the two roots is positive, hence $\Omega^+ > 0$. The property $\Omega^+ \times \Omega^- = A_0/A_4$ implies that $\Omega^- > 0$ in the case 1, and $\Omega^- < 0$ in the case 2. In summary, we get

$$\begin{cases} \omega^+ \in \mathbb{R}^+ & \forall k > 0, \\ \omega^- \in \mathbb{R}^+ & \text{if } (W'' > 0 \text{ or } k > k_c^e), \text{ else } \omega^- \in i\mathbb{R}. \end{cases} \quad (62)$$

The phase velocities $c_p^\pm(k) = \omega^\pm(k)/k$ of the fast wave and of the slow wave are deduced:

$$\begin{cases} c_p^+ \in \mathbb{R}^+ & \forall k > 0, \\ c_p^- \in \mathbb{R}^+ & \text{if } (W'' > 0 \text{ or } k > k_c^e), \text{ else } c_p^- \in i\mathbb{R}. \end{cases} \quad (63)$$

In the non-convexity interval $]\varepsilon_1, \varepsilon_2[$ and for long wavelengths ($k < k_c^e$), the slow wave does not propagate. In this case, ω^- is purely imaginary and $\tilde{\varepsilon} = \hat{\varepsilon} e^{|\omega^-|t} e^{-ikx}$ grows unbounded and in finite time comes out of $]\varepsilon_1, \varepsilon_2[$, which stabilizes the system. For $k \sim 0$, one has

$$c_p^+(k) \underset{0}{\sim} \sqrt{\frac{\lambda}{\beta}} \frac{1}{k}, \quad c_p^-(k) \underset{0}{\sim} \sqrt{\frac{W''}{\rho}} \text{ if } W'' > 0. \quad (64)$$

Thus, the phase velocity of the fast wave is singular at $k = 0$. If $W'' > 0$, we also deduce from (20) and (64) that $c_p^-(0) = c_p(0)$: the phase velocity of the master wave and of the slow wave are the same at the origin. This gives a meaning to the fast and slow waves:

- the slow wave is the physical wave, similar to the master wave,
- the fast wave is a spurious wave.

For large values of k , one has

$$c_p^+(k) \underset{+\infty}{\sim} \sqrt{\frac{W'' + \lambda}{\rho}} = \Lambda_e^{(2)}, \quad c_p^-(k) \underset{+\infty}{\sim} \sqrt{\frac{\alpha}{\beta}} = \Lambda_e^{(4)}, \quad (65)$$

where the eigenvalues $\Lambda_e^{(2,4)}$ are defined in (52): at infinite frequency, the phase velocities of the dispersive system tend towards the phase velocities of the non-dispersive system.

One last remark concerns the monotony of the slow wave. If $W'' \leq 0$, c_p^- is strictly increasing, like the master wave it mimics. On the other hand, if $W'' > 0$, the slow wave evolves

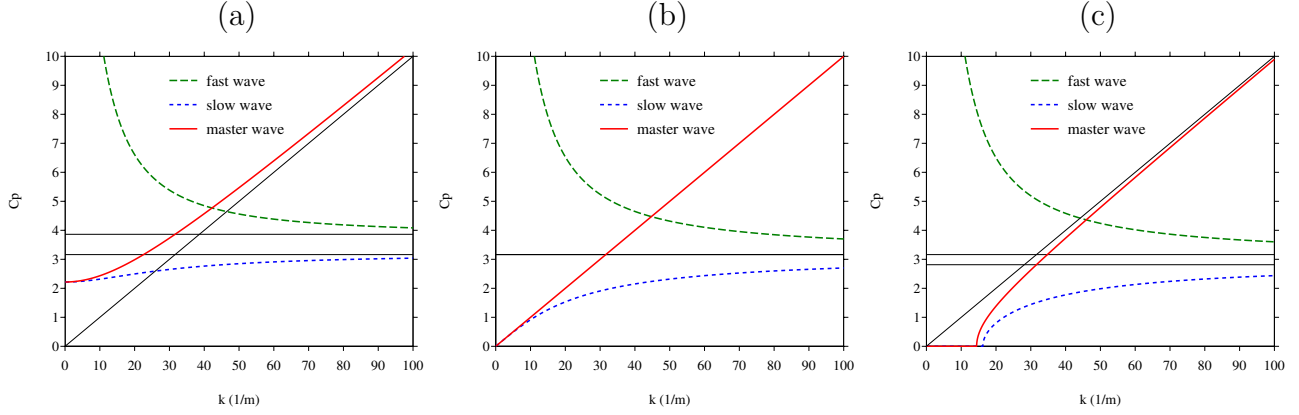


Figure 6: Fast wave phase velocity c_p^+ and slow wave phase velocity c_p^- of the extended Lagrangian, and phase velocity c_p of the master wave (20), for 3 values of $\bar{\varepsilon}$, leading to: $W'' > 0$ (a), $W'' = 0$ (b), and $W'' < 0$ (c). Horizontal lines designate eigenvalues $\Lambda_e^{(2,4)}$ (52). The line through the origin is the asymptote $\sqrt{\alpha/\rho}k$.

monotonously between $\sqrt{W''/\rho}$ at $k = 0$ and its asymptote $\Lambda_e^{(4)}$ for k tending towards $+\infty$. For the slow wave to be increasing when $W'' > 0$, like the master wave, the following inequality must therefore be satisfied:

$$\frac{\alpha}{\beta} > \frac{W''}{\rho}. \quad (66)$$

All these properties are illustrated in figure 6. The parameters are: $\rho = 1$, $\alpha = 10^{-2}$, $\lambda = 10$ and $\beta = 10^{-3}$. Three strain values are considered: $\bar{\varepsilon} = 0$ i.e. $W'' > 0$ (a), $\bar{\varepsilon} = \varepsilon_1$ i.e. $W'' = 0$ (b), $\bar{\varepsilon} = (\varepsilon_1 + \varepsilon_2)/2$ i.e. $W'' < 0$ (c). In case (a), the parameters satisfy (66), so that the slow wave is an increasing function of k .

4. Introduction of dissipation

To get closer to the real configurations, an energy dissipation mechanism is introduced into the evolution equations. To do this, we define the phenomenological dynamic viscosity $\mu > 0$ ($\text{kg.m}^{-1}.\text{s}^{-1}$).

4.1. Master Lagrangian

The dissipation is introduced through a Kelvin-Voigt model in the original system. The system (3) becomes

$$\begin{cases} \partial_t \varepsilon - \partial_x v = 0, & (67a) \\ \rho \partial_t v - \partial_x \sigma = \mu \partial_{xx}^2 v. & (67b) \end{cases}$$

The energy conservation law (5) writes

$$\partial_t E - \partial_x \Pi = -\mu (\partial_x v)^2, \quad (68)$$

where the Poynting term (6) is modified

$$\Pi = v \sigma + \alpha \partial_t \varepsilon \partial_x \varepsilon - \mu v \partial_x v. \quad (69)$$

Denoting by \mathcal{D} the dissipation of energy

$$\mathcal{D} = \int_0^L \mu (\partial_x v)^2 dx \geq 0, \quad (70)$$

the balance of energy (8) writes

$$\frac{d}{dt} \mathcal{E} = \mathcal{P} - \mathcal{D}. \quad (71)$$

The dimensional analysis performed in section 2.4 is slightly modified by the introduction of dissipation: the width of front D is unchanged, whereas the propagation speed of the front V becomes

$$V = \Phi_V \left(\sqrt{\frac{a_i}{\rho}}, \frac{\sqrt{a_i \alpha}}{\mu} \right), \quad (72)$$

where Φ_V is an unknown function.

4.2. Extended Lagrangian

Evolution equations. The dissipation is described here by a relaxation term, which does not change the structure of the PDEs. The system (30) becomes

$$\begin{cases} \partial_t \varepsilon - \partial_x v = 0, & (73a) \end{cases}$$

$$\begin{cases} \rho \partial_t v - \partial_x \sigma_e = 0, & (73b) \end{cases}$$

$$\begin{cases} \partial_t \eta = w, & (73c) \end{cases}$$

$$\begin{cases} \partial_t p - \partial_x w = 0, & (73d) \end{cases}$$

$$\begin{cases} \beta \partial_t w - \partial_x (\alpha p) = \lambda (\varepsilon - \eta) - \mu w. & (73e) \end{cases}$$

The conservation law of energy (34) becomes

$$\partial_t E_e - \partial_x \Pi_e = -\mu w^2. \quad (74)$$

Denoting by \mathcal{D}_e the dissipation of energy

$$\mathcal{D}_e = \int_0^L \mu w^2 dx \geq 0, \quad (75)$$

the energy balance (38) writes

$$\frac{d}{dt} \mathcal{E}_e = \mathcal{P}_e - \mathcal{D}_e. \quad (76)$$

Injecting (73e) into (73b), one notices that

$$\rho \partial_t v - \partial_x \left(W'(\varepsilon) - \alpha \partial_{xx}^2 \eta \right) = \mu \partial_{xt}^2 \eta + \beta \partial_{xtt}^3 \eta. \quad (77)$$

When $\lambda \rightarrow +\infty$ and $\beta \rightarrow 0$, then $\eta \rightarrow \varepsilon$ and one recovers (67b).

Dispersion analysis. The dispersion relation (57) becomes

$$A_4 \omega^4 + A_3 \omega^3 + A_2 \omega^2 + A_1 \omega + A_0 = 0 \quad (78)$$

with A_4 , A_2 et A_0 unchanged (58), whereas

$$A_3 = -i \rho \mu, \quad A_1 = i \mu (W'' + \lambda) k^2. \quad (79)$$

Relaxation matrix. The angular frequency (46) is supplemented by the characteristic frequency ν , as well as the critical values μ^* and δ :

$$\nu = \frac{\mu}{2\beta}, \quad \mu^* = 2\sqrt{\beta\lambda}, \quad \delta = \left(1 - \left(\frac{\nu}{\omega_0}\right)^2\right)^{1/2}. \quad (80)$$

If $\mu \leq \mu^*$, then $\nu \leq \omega_0$ and $\delta \in \mathbb{R}$. The relaxation matrix (48) becomes

$$\mathbf{S}_e = \begin{pmatrix} 0 & 0 & 0 & 0 & 0 \\ 0 & 0 & 0 & 0 & 0 \\ 0 & 0 & 0 & 0 & 1 \\ 0 & 0 & 0 & 0 & 0 \\ \omega_0^2 & 0 & -\omega_0^2 & 0 & -2\nu \end{pmatrix}, \quad (81)$$

The eigenvalues of \mathbf{S}_e are then 0 (at multiplicity 3) and $-\nu \pm i\delta\omega_0$. The dissipation does not modify the spectral radius (50). Based on (55), one obtains

$$\mathbf{M}_e \mathbf{S}_e = \tilde{\mathbf{S}}_e - 2\nu\beta\tilde{\mathbf{I}}_5, \quad (82)$$

where $\tilde{\mathbf{S}}_e$ is skew-symmetric, and $\tilde{\mathbf{I}}_5$ is the diagonal matrix whose only nonzero term is the diagonal entry $[\tilde{\mathbf{I}}_5]_{5,5} = 1$. This decomposition is consistent with the dissipation of energy [1].

5. Numerical modeling

The system (73) is a standard hyperbolic system with source term, that can be solved by the user's favorite scheme. The following section describes the numerical methodology chosen to obtain the numerical results presented in section 6.

5.1. Splitting

To integrate (49), a uniform spatial mesh $\Delta x = L/N_x$ and a variable time step $\Delta t^{(n)} \equiv \Delta t$ are introduced. An approximation \mathbf{U}_i^n of the exact solution $\mathbf{U}_e(x_i = i\Delta x, t_n = t_{n-1} + \Delta t)$ is sought. A naive explicit integration yields a bound of the form

$$\Delta t \leq \min\left(\frac{\Delta x}{c_{\max}}, \frac{2}{\varrho(\mathbf{S}_e)}\right), \quad (83)$$

where $c_{\max} = \max_i c_i^n$ is the maximal eigenvalue (52) at time t_n , and $\varrho(\mathbf{S}_e)$ is the spectral radius of the relaxation matrix \mathbf{S}^e (50). As deduced from (46), the second bound in (83) is penalizing compared with the standard CFL condition $\Delta t \leq \Delta x/c_{\max}$ when $\lambda \rightarrow +\infty$.

Here we follow another strategy: the system (49) is split into a propagation step

$$\partial_t \mathbf{U}_e + \partial_x \mathbf{f}_e(\mathbf{U}^e) = \mathbf{0} \quad (84)$$

and a relaxation step

$$\partial_t \mathbf{U}_e = \mathbf{S}_e \mathbf{U}_e. \quad (85)$$

The discrete operators associated with the discretization of (84) and (85) are denoted \mathbf{H}_p and \mathbf{H}_r , respectively. The second-order Strang splitting is used, solving successively (84) and (85) with adequate time increments:

$$\begin{cases} \mathbf{U}_i^{(1)} = \mathbf{H}_r \left(\frac{\Delta t}{2} \right) \mathbf{U}_i^n, & (86a) \\ \mathbf{U}_i^{(2)} = \mathbf{H}_p (\Delta t) \mathbf{U}_i^{(1)}, & (86b) \\ \mathbf{U}_i^{n+1} = \mathbf{H}_r \left(\frac{\Delta t}{2} \right) \mathbf{U}_i^{(2)}. & (86c) \end{cases}$$

Provided that \mathbf{H}_p and \mathbf{H}_r are second-order accurate and stable operators, the time-marching (86) gives a second-order accurate approximation of (49) [21].

In the previous sections, it has been shown that the energy \mathcal{E}_e is conserved or decreases if the power of the boundary efforts is zero (45). Furthermore, if the solutions are smooth and the dissipation is zero, then the energy \mathcal{E}_e is conserved. To check these properties numerically, an approximation of the energy (35)-(37) is computed at each time step:

$$\mathcal{E}_e^n = \Delta x \sum_{i=0}^{N_x} \left(\frac{\rho}{2} (v_i^n)^2 + \frac{\beta}{2} (w_i^n)^2 + W(\varepsilon_i^n) + \frac{\alpha}{2} (p_i^n)^2 + \frac{\lambda}{2} (\varepsilon_i^n - \eta_i^n)^2 \right). \quad (87)$$

5.2. Propagation step

The propagation step (84) is solved by a conservative scheme for hyperbolic systems [28]:

$$\mathbf{U}_i^{n+1} = \mathbf{U}_i^n - \frac{\Delta t}{\Delta x} (\mathbf{F}_{i+1/2} - \mathbf{F}_{i-1/2}). \quad (88)$$

Here we use a finite-volume scheme with flux limiters [21]. This scheme has a stencil of width 2, and it is stable under the usual Courant-Friedrichs-Lewy (CFL) condition

$$\Delta t = \frac{\gamma \Delta x}{c_{\max}}, \quad \text{with } \gamma \leq 1. \quad (89)$$

The numerical flux $\mathbf{F}_{i+1/2}$ requires to approximate the Jacobian matrix $\mathbf{f}'_e(\mathbf{U}_{i+1/2})$ (51) at the midpoint of $[x_i, x_{i+1}]$ and at time t_n . For this purpose, one seeks the Roe matrix $\mathbf{A}_{i+1/2}$ which satisfies [21]:

1. $\mathbf{A}_{i+1/2}$ is diagonalizable with real eigenvalues;
2. $\mathbf{A}_{i+1/2} (\mathbf{U}_{i+1}^n - \mathbf{U}_i^n) = \mathbf{f}_e(\mathbf{U}_{i+1}^n) - \mathbf{f}_e(\mathbf{U}_i^n)$;
3. $\lim_{\mathbf{U}_{i+1}^n \rightarrow \mathbf{U}_i^n} \mathbf{A}_{i+1/2} = \mathbf{f}'_e(\mathbf{U}_i^n)$.

According to section 15.3.2 of [21], such a matrix may be expressed by the formula

$$\mathbf{A}_{i+1/2} = \int_0^1 \mathbf{f}'_e(\mathbf{U}_i^n + s(\mathbf{U}_{i+1}^n - \mathbf{U}_i^n)) ds, \quad (90)$$

which ensures that the properties 2 and 3 are satisfied. As in exercise 15.1.(a) p. 349 of [21], the Roe matrix is deduced from (51):

$$\mathbf{A}_{i+1/2} = \begin{pmatrix} 0 & -1 & 0 & 0 & 0 \\ -\frac{\kappa_{i+1/2} + \lambda}{\rho} & 0 & \frac{\lambda}{\rho} & 0 & 0 \\ 0 & 0 & 0 & 0 & 0 \\ 0 & 0 & 0 & 0 & -1 \\ 0 & 0 & 0 & -\frac{\alpha}{\beta} & 0 \end{pmatrix}, \quad (91)$$

where

$$\kappa_{i+1/2} = \begin{cases} \frac{W'(\varepsilon_{i+1}^n) - W'(\varepsilon_i^n)}{(\varepsilon_{i+1}^n - \varepsilon_i^n)} & \text{if } \varepsilon_{i+1} \neq \varepsilon_i, \\ W''(\varepsilon_i^n) & \text{else.} \end{cases} \quad (92)$$

The rest of the scheme is fully described in [21] and in Appendix A of [31].

To discretize (44), we introduce ghost-cell values before the propagative step (88). Following [21], these ghost values denoted by stars are, on the left boundary ($j = 1, 2$),

$$\begin{cases} \varepsilon_{-j}^* = +\varepsilon_j^n, \end{cases} \quad (93a)$$

$$\begin{cases} v_{-j}^* = 2f_v(t_n) - v_j^n, \end{cases} \quad (93b)$$

$$\begin{cases} \eta_{-j}^* = +\eta_j^n, \end{cases} \quad (93c)$$

$$\begin{cases} p_{-j}^* = -p_j^n, \end{cases} \quad (93d)$$

$$\begin{cases} w_{-j}^* = +w_j^n. \end{cases} \quad (93e)$$

On the right boundary, the ghost values are ($j = 1, 2$)

$$\begin{cases} \varepsilon_{N_x+j}^* = 2f_\varepsilon(t_n) - \varepsilon_{N_x-j}^n, \end{cases} \quad (94a)$$

$$\begin{cases} v_{N_x+j}^* = v_{N_x-j}^n, \end{cases} \quad (94b)$$

$$\begin{cases} \eta_{N_x+j}^* = 2f_\eta(t_n) - \eta_{N_x-j}^n, \end{cases} \quad (94c)$$

$$\begin{cases} p_{N_x+j}^* = -p_{N_x-j}^n, \end{cases} \quad (94d)$$

$$\begin{cases} w_{N_x+j}^* = 2f_w(t_n) - w_{N_x-j}^n. \end{cases} \quad (94e)$$

5.3. Relaxation step

The relaxation step (85) is an ODE with constant coefficients. The exact operator in (86a)-(86c) is

$$\mathbf{H}_r(\tau) \mathbf{U}_i = \exp(\mathbf{S}_e \tau) \mathbf{U}_i \equiv \mathbf{N}(\tau) \mathbf{U}_i, \quad (95)$$

with $\tau = \Delta t/2$. In the conservative case $\mu = 0$, the exponential matrix is

$$\mathbf{N}(\tau) = \begin{pmatrix} 1 & 0 & 0 & 0 & 0 \\ 0 & 1 & 0 & 0 & 0 \\ 1 - \cos \omega_0 \tau & 0 & \cos \omega_0 \tau & 0 & \frac{1}{\omega_0} \sin \omega_0 \tau \\ 0 & 0 & 0 & 1 & 0 \\ \omega_0 \sin \omega_0 \tau & 0 & -\omega_0 \sin \omega_0 \tau & 0 & \cos \omega_0 \tau \end{pmatrix}. \quad (96)$$

In the case of small dissipation $\mu \leq \mu^*$ (80), then $\delta \in \mathbb{R}$ and the non-null components of \mathbf{N} are

$$\begin{aligned}
\mathbf{N}[1, 1] &= \mathbf{N}[2, 2] = \mathbf{N}[3, 3] = 1, \\
\mathbf{N}[3, 1] &= 1 - e^{-\nu t} \left(\cos \delta \omega_0 \xi + \frac{\nu}{\delta \omega_0} \sin \delta \omega_0 \xi \right), \\
\mathbf{N}[3, 3] &= e^{-\nu t} \left(\cos \delta \omega_0 \xi + \frac{\nu}{\delta \omega_0} \sin \delta \omega_0 \xi \right), \\
\mathbf{N}[3, 5] &= \frac{1}{\delta \omega_0} e^{-\nu t} \sin \delta \omega_0 \xi, \\
\mathbf{N}[5, 1] &= -\mathbf{N}[5, 3] = \frac{\omega_0}{\delta} e^{-\nu t} \sin \delta \omega_0 \xi, \\
\mathbf{N}[5, 5] &= e^{-\nu t} \left(\cos \delta \omega_0 \xi - \frac{\nu}{\delta \omega_0} \sin \delta \omega_0 \xi \right).
\end{aligned} \tag{97}$$

When $\mu \rightarrow 0$, then (97) recovers (96).

5.4. Estimation of λ and β

The extended Lagrangian is constructed so that its solution tends towards the solution of the master Lagrangian model when $\lambda \rightarrow +\infty$ and $\beta \rightarrow 0$. It remains to determine the finite and non-zero values of these parameters during numerical simulations. This choice is based on the theoretical analysis of the extended system (sections 3.2 and 3.3) and on numerical analysis criteria (section 5.2):

- the penalization parameter must satisfy $\lambda \geq \lambda_{\min} = 25/12$ to ensure that the system (30) is unconditionally hyperbolic;
- if $W'' \geq 0$, the inequality (66) must be satisfied. This inequality depends on $\bar{\varepsilon}$ (strain around which the equations are linearized) and therefore does not lead to a solution-independent bound. Assuming $\bar{\varepsilon} \in [0, \varepsilon_2^0]$, we get $\max W'' = W''(0) = 2a_2$. We deduce a lower bound from the dimensionless number Γ :

$$\Gamma = \frac{\rho}{2a_2} \frac{\alpha}{\beta} \geq 1, \tag{98}$$

hence an upper bound for β . A finer bound can be obtained by defining the maximum wave number resolved by the extended system $k^* = 2\pi/\ell^*$. A necessary condition for the slow wave to converge to the phase velocity of the master wave over this interval is then $\Lambda^{(4)}(k) \geq c_p(k)$ if $k \in [0, k^*]$. Hence

$$\Gamma \geq 1 + \frac{2\pi^2 \alpha}{a_2 (\ell^*)^2}. \tag{99}$$

- if $W'' < 0$, the error on the critical wave numbers (21) and (60) depends only on λ :

$$\begin{aligned}
\left| \frac{k_c^e}{k_c} - 1 \right| &= \frac{1}{\sqrt{1 + W''/\lambda}}, \\
&\leq \frac{1}{2\lambda} \left| W''_{\min} \right|, \\
&\leq \frac{25}{24} \frac{1}{\lambda}.
\end{aligned} \tag{100}$$

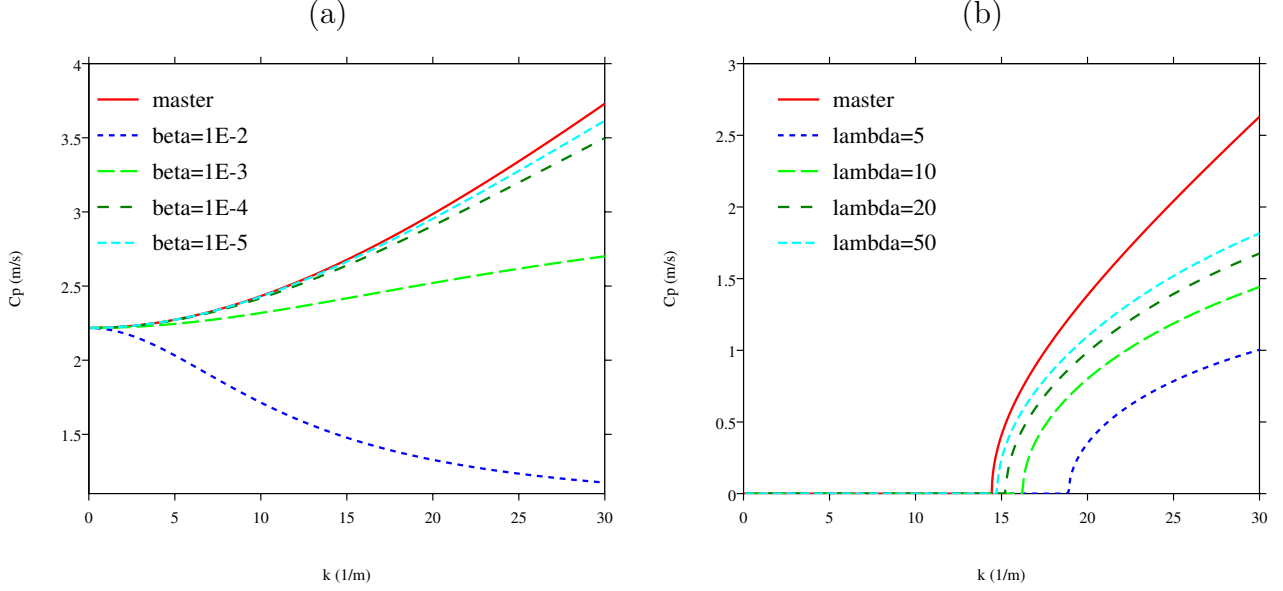


Figure 7: Phase velocities of the master wave c_p (20) and of the slow wave c_p^- . (a): $W'' > 0$, $\lambda = 100$ and various values of β . (b): $W'' < 0$, $\beta = 10^{-3}$ and various values of λ .

On the other hand, numerical arguments come into play. The eigenvalues (52) satisfy $\Lambda^{(2)} = \mathcal{O}(\sqrt{\lambda})$ and $\Lambda^{(4)} = \mathcal{O}(1/\sqrt{\beta})$. By the stability condition CFL (89), we have $\Delta t = \mathcal{O}(\sqrt{\lambda} + 1/\sqrt{\beta})$: increasing λ and decreasing β decreases the time step and consequently increases the duration of the simulations. Moreover, $\Lambda_e^{(2)} \sim \Lambda_e^{(4)}$ minimizes the numerical dissipation of the slow wave. By equating these two eigenvalues for $W'' = 0$, we get

$$\lambda + 2a_2 = \rho \frac{\alpha}{\beta}, \quad (101)$$

and hence

$$\lambda \geq \lambda_c = \max(\lambda_{\min}, 2a_2(\Gamma - 1)). \quad (102)$$

Figure 7 illustrates the role of λ and β on the dispersion curves. In (a), the influence of the choice of β in (98) is illustrated for $\bar{\varepsilon} = 0$, i.e. $W'' > 0$, and $\lambda = 100$. For $\beta = 10^{-2}$, we have $\Gamma = 0.4 < 1$ and c_p^- decreases, contrary to c_p : the solution of the extended Lagrangian does not converge towards the solution of the master Lagrangian. The agreement improves as β decreases.

In figure 7-(b), the strain is $\bar{\varepsilon} = (\varepsilon_1 + \varepsilon_2)/2$, or $W'' < 0$; we choose $\beta = 10^{-3}$, or $\lambda_c \approx 18$ (102). The agreement between c_p and c_p^- improves as λ increases, especially the position of the cutoff wave numbers (100). However, this improvement is limited: unlike c_p , an asymptote dependent on β upper bounds c_p^- .

6. Numerical experiments

6.1. Riemann problem

Here we illustrate the dynamics obtained by competition between nonlinear and dispersive effects. We also study the influence of the parameters β and λ on the convergence of the extended Lagrangian. The domain $[-2, 2]$ is discretized on $N_x = 1600$ computation points. The

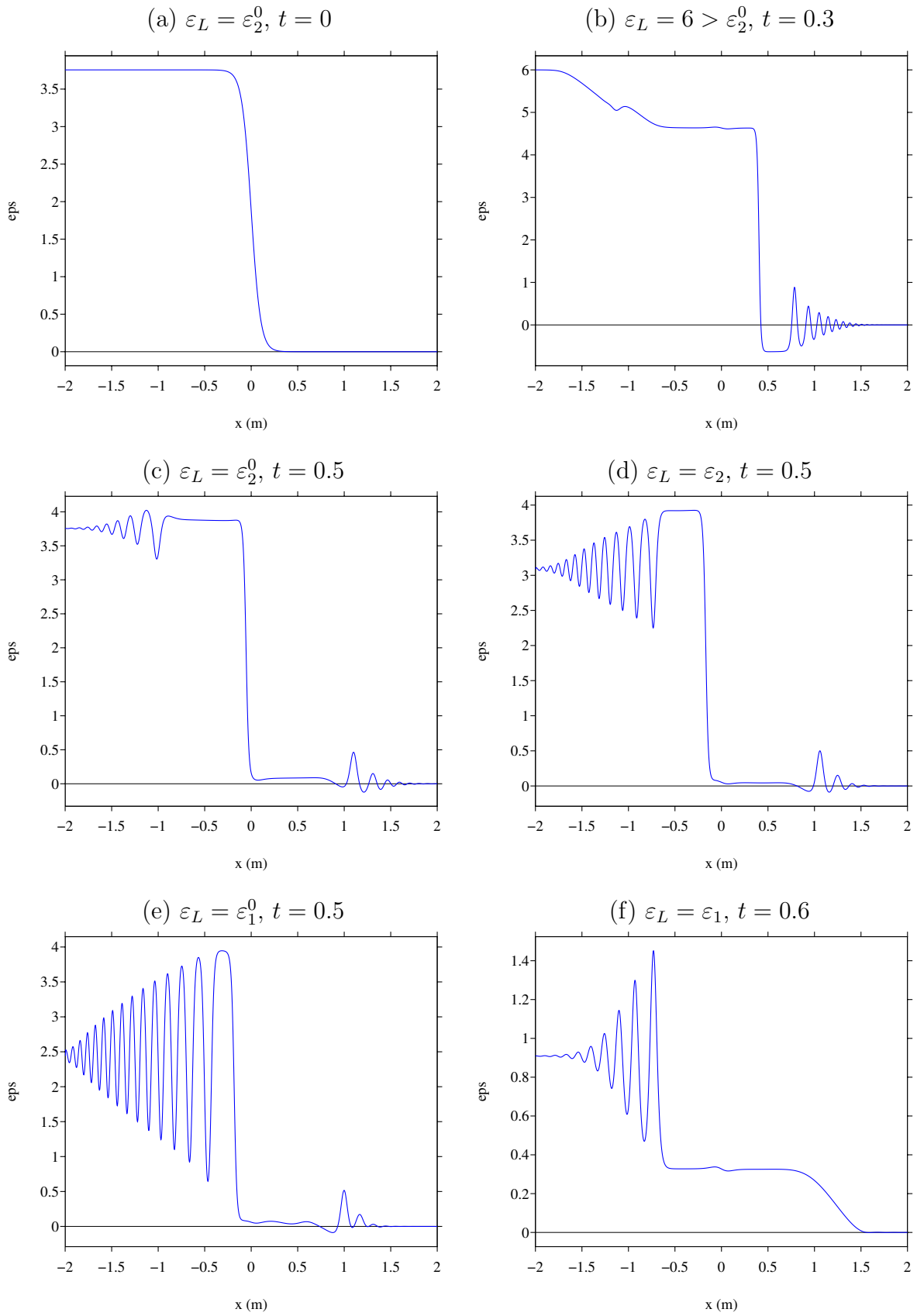


Figure 8: Solution ε of the Riemann problem (103), for various values of ε_L . (a): initial data $\varepsilon_0(x)$ in (103), where $\zeta = 0.1$, $x_0 = 0$ and $\varepsilon_L = \varepsilon_2^0$. (b): $\varepsilon_L = 6 > \varepsilon_2^0$. (c): $\varepsilon_L = \varepsilon_2^0$. (d): $\varepsilon_L = \varepsilon_2$. (e): $\varepsilon_L = \varepsilon_1^0$. (f): $\varepsilon_L = \varepsilon_1$.

grid is fine enough so that the solutions are independent of the computing grid. The CFL number is $\gamma = 0.95$ (89).

The parameters of the extended Lagrangian (35) are $\rho = 1$, $\alpha = 10^{-3}$, $\beta = 10^{-5}$ and $\lambda = 100$. The criteria given in section 5.4 are satisfied: $\Gamma = 40 \gg 1$ (98) and $\lambda > \lambda_c = 15$ (102). Attenuation is not taken into account: $\mu = 0$ in (73). The initial data (39) are constructed from two constant states linked in $x_0 = L/2$ by a regularizing function:

$$\mathbf{U}_0(x) = \frac{1}{2} (\mathbf{U}_R + \mathbf{U}_L) + \frac{1}{2} (\mathbf{U}_R - \mathbf{U}_L) \tanh\left(\frac{x - x_0}{\zeta}\right), \quad (103)$$

where $\zeta = 0.1$. This regularization eliminates the initial discontinuity, which is not admissible in the master Lagrangian model (6). The left and right states are $\mathbf{U}_L = (\varepsilon_L, 0, 0)^\top$ and $\mathbf{U}_R = \mathbf{0}$. The simulations are stopped before the waves reach the edges of the domain, where the values are kept constant. Figure 8-(a) displays $\varepsilon_0(x)$ with $\varepsilon_L = \varepsilon_2^0$.

Figure 8 represents the solution ε of (103) for decreasing values of the initial data ε_L (table 1): $6 > \varepsilon_2^0$ at $t = 0.3$ s (b), ε_2^0 at $t = 0.5$ s (c), ε_2 at $t = 0.5$ s (d), ε_1^0 at $t = 0.5$ s (e), ε_1 at $t = 0.6$ s (f). When $\varepsilon_L = 6$ (b), a front propagates to the right preceded by oscillations; on the left a smooth structure propagates. At the bistability point ε_2^0 (c), the front remains stationary and generates dispersive waves; in the case of a discontinuity $\zeta = 0$ (not shown here), no waves are generated. For smaller values of ε (d,e,f), the front propagates to the left and tends towards a dispersive shock wave.

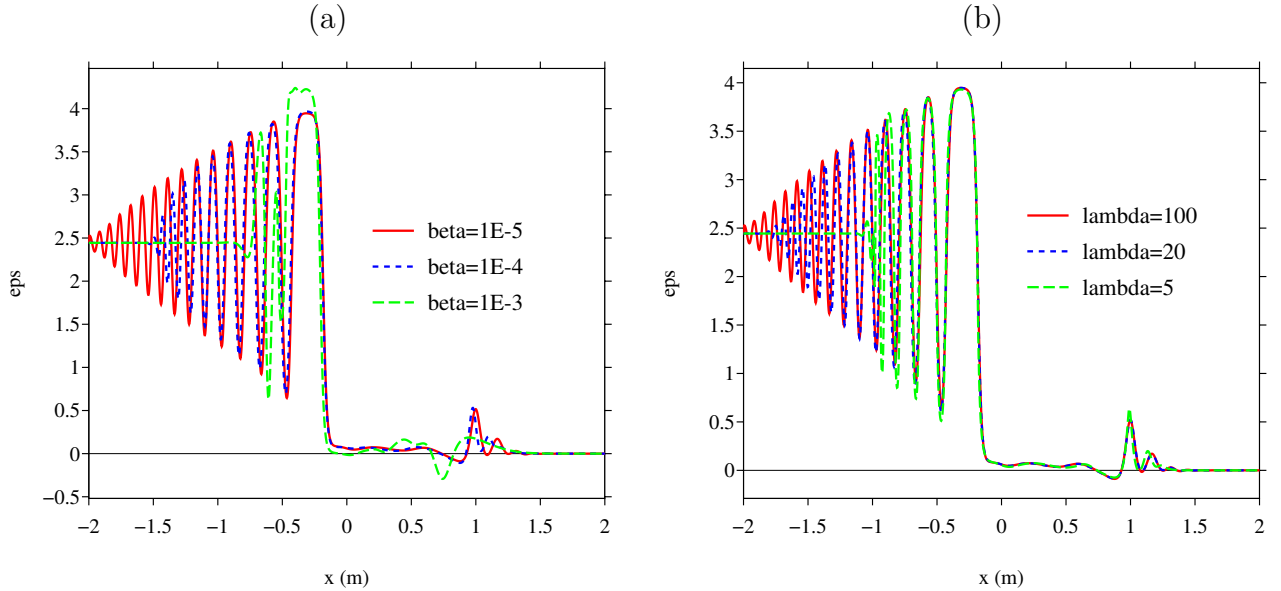


Figure 9: Evolution of the solution to the Riemann problem (103) in terms of β and λ , for $\varepsilon_L = \varepsilon_1^0$ at $t = 0.5$. (a): β variable and $\lambda = 100$. (b): λ variable and $\beta = 10^{-5}$.

Figure 9 illustrates the influence of β and λ on the solution of the extended Lagrangian. The initial data is $\varepsilon_L = \varepsilon_1^0$ and the final time is $t = 0.5$ s, which corresponds to the figure 8-(d). In (a), the solution obtained with $\beta = 10^{-5}$ is indistinguishable from solutions obtained with smaller values of β (not shown here) and can be considered as the reference solution. For $\beta = 10^{-4}$, the agreement with this reference solution is correct, except for the fastest waves.

For $\beta = 10^{-3}$, we have $\Gamma = 0.4 < 1$: the criterion (98) is not satisfied, and the solution has not converged to the reference solution.

In figure 9-(b), we choose $\beta = 10^{-5}$, and several values of λ are considered. The reference solution obtained with $\lambda = 100$ cannot be distinguished from solutions obtained for larger values of λ (not shown here). For smaller values of λ , agreement with the reference solution is degraded, especially for $\lambda = 5 < \lambda_c = 18$ (102). Similar convergence studies were carried out with all the values of ε_L shown in figure 8 and led to the same conclusions: subsequently, the solutions obtained with $\beta = 10^{-5}$ and $\lambda = 100$ are considered as the reference for the extended Lagrangian.

6.2. Variable boundary conditions

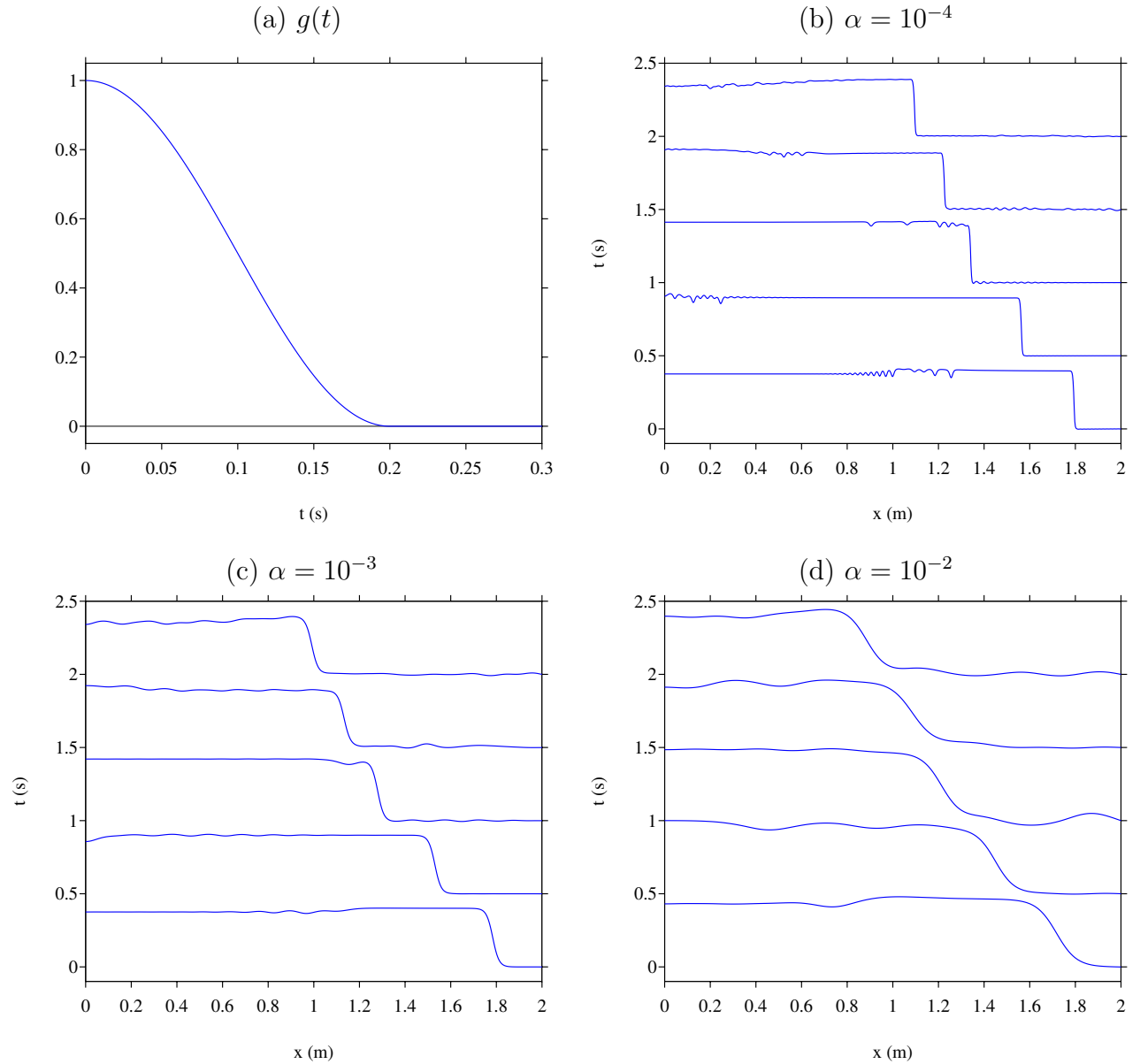


Figure 10: Variable boundary conditions. (a): forcing $g(t)$ in (104)-(105), with $f_c = 5$ Hz. (b,c,d): snapshots of ε at successive instants and for various values of the regularization parameter α .

We mimic a real experiment where the second equilibrium state ε_2^0 is perturbed by a time-varying boundary condition (40). For this, the forcings in (44a) and (44c) are chosen as

$$f_v(t) = 0, \quad f_\eta(t) = \varepsilon_2^0 g(t), \quad \text{with } g(t \leq 0) = 1. \quad (104)$$

From (32) and (104), we can reformulate the forcings (44d) and (44e): $f_\varepsilon(t) = s^{-1}(s(\varepsilon_2^0)g(t))$ and $f_w(t) = \varepsilon_2^0 g'(t)$. The function evolves smoothly between two constant states 1 and 0:

$$g(t) = \begin{cases} 1 & \text{if } t \leq 0, \\ \frac{1}{2}(1 + \cos(\pi f_c t)) & \text{if } 0 < t \leq 1/f_c, \\ 0 & \text{if } t > 1/f_c, \end{cases} \quad (105)$$

as sketched in figure 10-(a). The characteristic times are the period of the forcing $T_c = 1/f_c$ (105) and the relaxation time $T_0 = 2\pi/\omega_0$ (46). The ratio between these time scales is

$$\theta = \frac{T_c}{T_0} = \frac{1}{2\pi f_c} \sqrt{\frac{\lambda}{\beta}}. \quad (106)$$

We choose $f_c = 5$ Hz in (105), so that $\theta = 100$ when $\lambda = 100$ and $\beta = 10^{-5}$: the forcing is quasi-static. When $\theta \rightarrow +\infty$, the system becomes stiff, which raises numerical issues [21].

The domain $[0, L]$ is discretized on 800 grid nodes, with $L = 2$. The following numerical experiments have been validated by checking the independence of the solutions with respect to the numerical parameters. Moreover, it has been verified that the discrete energy (87) grows as long as the source is turned on, and afterwards remains almost constant.

Figure 10-(b,c,d) displays snapshots of ε at successive instants $t_n = n/2$, with $n = 1, \dots, 5$, and for different values of the regularization parameter α . We choose $\lambda = 100$ and $\beta = \alpha/100$, as deduced from the numerical experiments in section 6.1. At the first instant represented ($t = 0.5$ s), the source is turned off: by (44c)-(44d), we have $\varepsilon(L, t) = \eta(L, t) = 0$. For all values of α , we observe that a front has separated from the right border $x = L$ and propagates to the left when t increases. This front is preceded by ripples, which are reflected by the left border $x = 0$ and cross the main front; they then slow it down.

One can notice that before the interaction with the reflected waves on the left border ($t = 0.5$ s in Figure 10-(b,c,d)), the height of the constant state on to the left of the front is greater than the initial value of ε . In addition, the width of the front D and its propagation speed V are all the greater as α is large, which is consistent with the dimensional analysis (72).

Figure 11 illustrates the influence of the energy dissipation on the propagation of the front. The parameters are $\alpha = 10^{-3}$, $\beta = 10^{-5}$ and $\lambda = 100$. Four values of μ in (73) are considered: $\mu = 0$ (no dissipation), $1/100$, $1/50$ and $1/20$. All these values are smaller than $\mu^* = 1/15.8$ in (80), so that the matrix exponential in the splitting is given by (97). In (a), we present ε at $t = 1$ s; at this instant, the ripples preceding the main front in the case $\mu = 0$ have reached the left edge in $x = 0$ and are reflected. We observe that the propagation speed of the front decreases when the attenuation parameter μ increases, which is consistent with the dimensional analysis (22). In addition, attenuation eliminates ripples and decreases the amplitude of the plateau in advance of the front. For high attenuation ($\mu = 1/20$), the shape of the front is sharpened. Figure 11-(b) represents the temporal evolution of the discrete energy (87). In the conservative case ($\mu = 0$), the mechanical energy increases up to t_c , due to the power of the

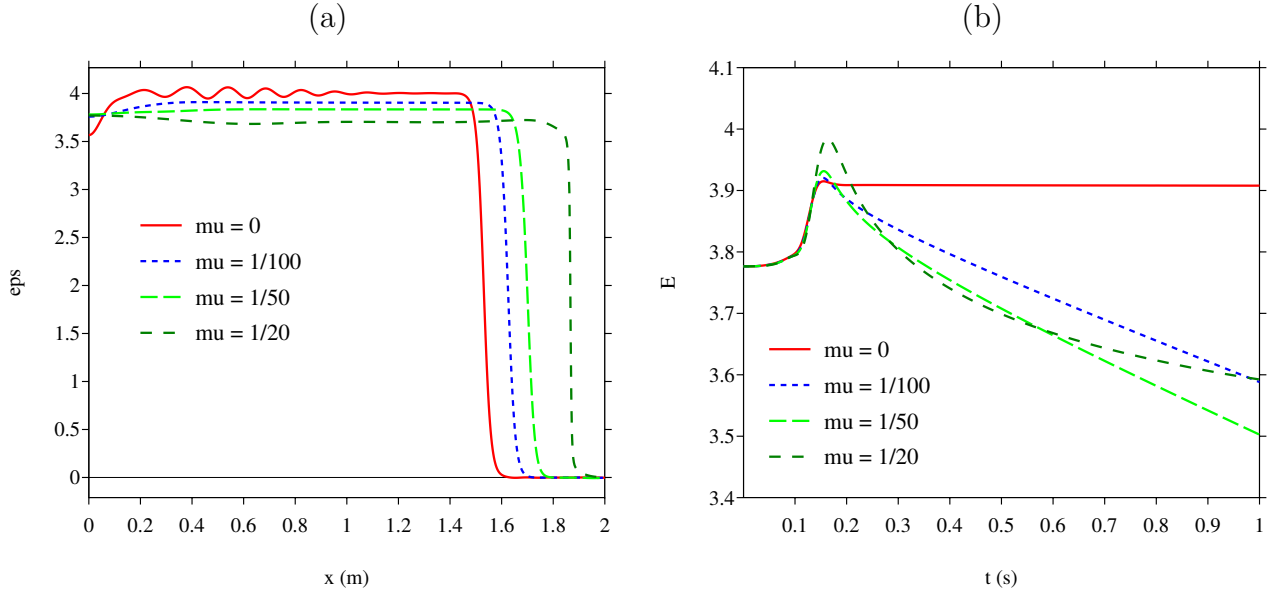


Figure 11: Variable boundary conditions (104)-(105): influence of the dissipation parameter μ in (73e). (a) snapshots of ϵ at $t = 1$ s. (b) time evolution of the discrete energy (87).

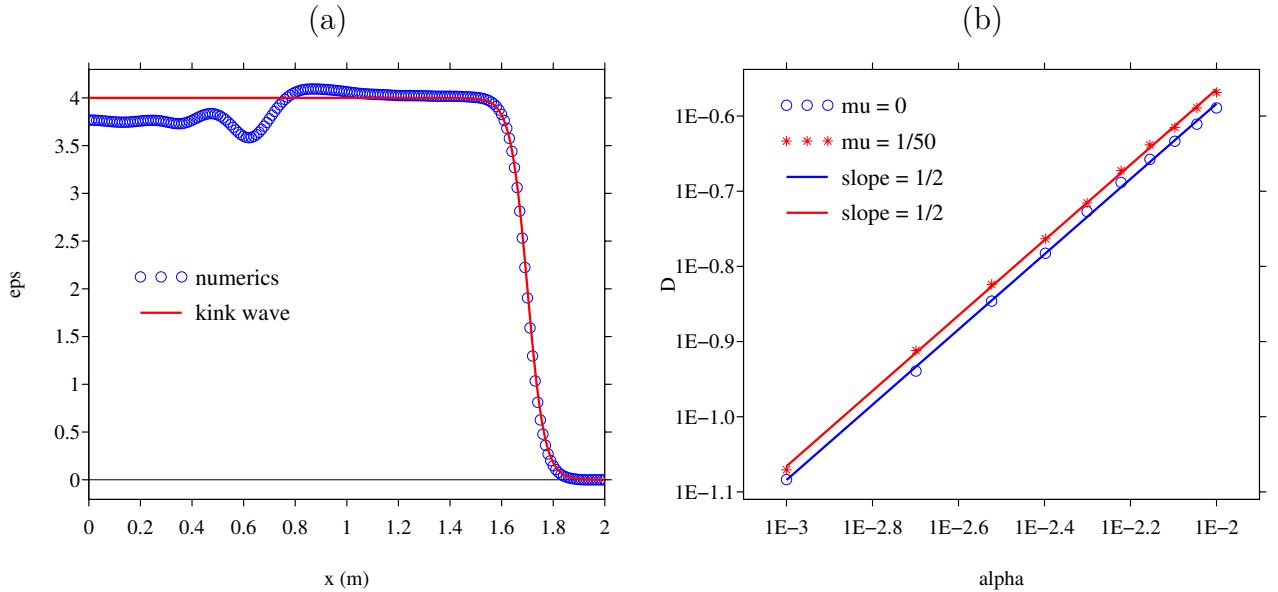


Figure 12: Variable boundary conditions (104)-(105): influence of the regularization parameter α on the shape of the front. (a): comparison between the numerical solution and the kink wave (27), at $t = 0.6$ s and for $\alpha = 5 \cdot 10^{-3}$. (b) log-log plot of D vs α , for two values of μ , and linear regression with slopes $1/2$.

forces applied at $x = L$ (45). For $t > t_c$, this power is null and the discrete energy is preserved (at the scale of the figure). When $\mu > 0$, the energy is dissipated after t_c .

In figure 12, we study quantitatively the influence of the regularization parameter α on the width D of the front. Given α , we choose $\beta = \alpha/100$, $\lambda = 100$, and $\mu = 0$ (no dissipation) or $\mu = 1/50$. Simulations are stopped at $t = 0.6$ s, before the signal reflected by the left edge interacts with the front. In figure 12(a), we compare the numerical value of ϵ to the theoretical

profile of the kink wave (27); the data are $t = 0.6$ s, $\alpha = 5.10^{-3}$, and $\mu = 0$. The agreement is very good about the shape and height of the constant states surrounding the front. The differences observed on the zone $[0, 1]$ are logically due to the fact that the initial value $\varepsilon_2^0 < \varepsilon_L$ cannot be connected to $\varepsilon_R = 0$ by a kink wave.

For each simulation, one determines the zone such that $\varepsilon \in [0.05 \varepsilon_R, 0.95 \varepsilon_L]$, where $\varepsilon_{R,L}$ are the values of the constant states on the right and left of the front respectively; typically, $\varepsilon_R = 0$ and $\varepsilon_L = 4$ when $\mu = 0$ (section 2.4). This zone allows to estimate D . In figure 12-(b), we represent D for $\alpha \in [10^{-3}, 10^{-2}]$ in a log-log scale. A linear least squares regression leads to a straight line with slope $1/2$, for the both values of μ . This specifies the property expected by dimensional analysis (22) and by the kink wave solution (28): $D \propto \sqrt{\alpha}$.

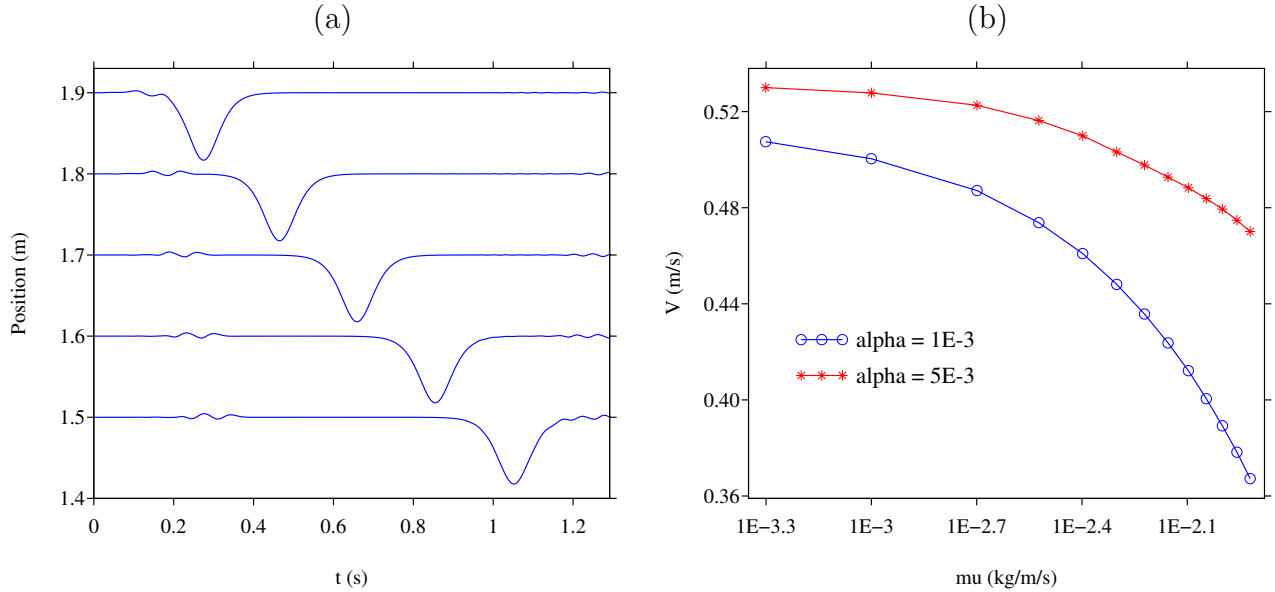


Figure 13: Variable boundary conditions (104)-(105): influence of the dissipation parameter μ and of the regularization parameter α on the speed V of the front. (a) time evolution of p at the receivers. (b) plot of V vs μ , for two values of α .

In figure 13, we study the influence of the dissipation parameter μ and of the regularization parameter α on the speed V of the front. For this purpose, $p = \partial_x \eta$ is recorded each time step at 5 receivers $x_r = 1.5 + 0.1 n$, with $n = 0, \dots, 4$. The field p allows to locate clearly the position of a front in η . In figure 13-(a), we represent the temporal evolution of p at these receivers, in the form of a seismogram. The spacing between these lines is constant, indicating that the velocity is constant. A linear regression on the position of the extrema allows to estimate the velocity of the front V . When $\mu = 0$, we measure $V = 0.5$ m/s, which corresponds exactly to the theoretical value for a kink wave (26). Moreover, the measured velocity is then independent of the regularization parameter α , as analysed in section 2.4.

In figure 13-(b), we represent V as a function of the dissipation parameter μ , for two values of α . For small values of μ , V tends towards 0.5 m.s^{-1} , which is the measured value without dissipation and theoretically predicted. We observe that V is a strictly decreasing function of μ , which was already noted in figure 11. It is also observed that, at a given μ , V increases with α . These observations are consistent with (22)-(72). Finally, we note that these data do not line up on a log-log scale, which indicates that there is no power law relating V to μ and α .

7. Conclusion

This work was focused on the dynamic behaviour of a regularized and bistable Ericksen bar. A Lagrangian has been proposed, combining a nonconvex energy and a regularization high-order term. This initial master Lagrangian was transformed into an extended Lagrangian to yield a hyperbolic nonlinear PDE system with source term, well adapted to numerical modelling. Comparisons between exact and numerical solutions demonstrated that the dynamics of the master Lagrangian is well captured by the extended Lagrangian.

Numerical results showed also that the regularized bistable Ericksen bar is able to reproduce the particular scenario of switching from one stable configuration to the other one by prescribing time-varying boundary conditions on higher order terms: at each time of the switching, the bar is a two-phase bar (the two phases corresponding locally to the two stable states) separated by a transition zone that moves at constant speed along the bar. In practice, this result is a starting point to design innovative deployable structures, by finding some metamaterials whose behaviour presents some analogies with a bistable regularized Ericksen bar.

Several theoretical issues now need to be addressed. The most important concerns the convergence of the solution of the extended Lagrangian towards the solution of the master Lagrangian when $\beta \rightarrow 0$ and $\lambda \rightarrow +\infty$. A similar analysis of the Serre-Green-Naghdi model was conducted in [6]. In this reference, the author proved that the initial data for the additional unknowns η and w had to be properly chosen to ensure convergence. It is likely that a similar property will need to be verified here.

A second direction of research concerns the theoretical and numerical analysis of the model (3) for general (and not necessarily polynomial) expressions of Ericksen energy. In the case of a piecewise linear energy, it has been proven in [17] that solitary waves are generated, or on the contrary that stop-band behaviors are obtained, depending on the slopes of the energy.

Lastly, the construction of transparent boundary conditions for dispersive equations of the form (30) is an active research topic. One can be inspired by [18] and references therein.

Acknowledgments. The authors acknowledge the stimulating exchanges promoted by the GDR MecaWave of the French CNRS, and the Labex MEC. They are also grateful to Sergey Gavriluk for fruitful discussion, and Marie Touboul for her careful reading. N. Favrie acknowledges the ANR-Astrid project SNIP grant number ANR-19-ASTR-0016-01 for partial funding.

References

- [1] C. BELLIS, B. LOMBARD, *Simulating transient wave phenomena in acoustic metamaterials using auxiliary fields*, Wave Motion 86 (2019), 175-194.
- [2] D. BRESCH, F. COUDERC, P. NOBLE, J.P. VILA, *A generalization of the quantum Bohm identity: Hyperbolic CFL condition for Euler-Korteweg equations*, Comptes Rendus Mathématiques, 354-1 (2016), 39-43.
- [3] R. DE PASCALIS, G. NAPOLI, G. SACCOMANDI, *Kink-type solitary waves within the quasi-linear viscoelastic model*, Wave Motion 86 (2019), 195-202.
- [4] F. DHAOUADI, N. FAVRIE, S. GAVRILYUK, *Extended Lagrangian approach for the defocusing nonlinear Schrödinger equation*, Stud. App. Math. 142-3 (2019), 336-358.

- [5] D. DIEHL, J. KREMSER, D. KRÖNER, C. ROHDE, *Numerical solution of Navier-Stokes-Korteweg systems by local discontinuous Galerkin methods in multiple space dimensions*, App. Math. Comput. 272 (2016), 309-335.
- [6] V. DUCHÊNE, *Rigorous justification of the Favrie-Gavrilyuk approximation to the Serre-Green-Naghdi model*, Nonlinearity 32 (2019)
- [7] J.L. ERICKSEN, *Equilibrium of bars*, J. Elasticity 5 (1975), 191-201.
- [8] J.L. ERICKSEN, *Introduction to the Thermodynamics of Solids*, Applied Mathematical Sciences 131, Springer (1998).
- [9] L.C. EVANS, *Partial Differential Equations*, Graduate Studies in Mathematics, American Mathematical Society (2010).
- [10] N. FAVRIE, S. GAVRILYUK, *A rapid numerical method for solving Serre-Green-Naghdi equations describing long free surface gravity waves*, Nonlinearity 30-7 (2017), 2718-2736.
- [11] J. GIESSELMANN, C. MAKRIDAKIS, T. PRYER, *Energy consistent discontinuous Galerkin methods for the Navier-Stokes-Korteweg system*, Math. Comput. 83-289 (2014), 2071-2099.
- [12] E. GODLEWSKI, P.A. RAVIART, *Numerical Approximation of Hyperbolic Systems of Conservation Laws*, Applied Mathematical Sciences 118, Springer-Verlag (1996).
- [13] S.D. GUEST, S. PELLEGRINO, *Analytical models for bistable cylindrical shells*, Proc. Royal Soc. A 462 (2006), 839-854.
- [14] F. GUINOT, S. BOURGEOIS, B. COCHELIN, L. BLANCHARD, *A planar rod model with flexible thin-walled cross-sections. Application to the folding of tape springs*, Int. J. Solids Struct. 49-1 (2012), 73-86.
- [15] S. HOFFAIT, O. BRULS, D. GRANVILLE, F. CUGNON, G. KERSCHEN, *Dynamic analysis of the self-locking phenomenon in tape-spring hinges*, Acta Astronaut., 66 (78) (2009), 1125-1132.
- [16] W. D. KALIES, P. J. HOLMES, *On a dynamical model for phase transformation in non-linear elasticity*, Fields Inst. Commun. 5 (1996), 255-269.
- [17] S. KATZ, S. GIVLI, *Solitary waves in a bistable lattice*, Extreme Mech. Lett. 22 (2018), 106-111.
- [18] M. KAZAKOVA, P. NOBLE, *Discrete transparent boundary conditions for the linearized Green-Naghdi system of equations*, submitted (2017).
- [19] O. LE MÉTAYER, S. GAVRILYUK, S. HANK, *A numerical scheme for the Green-Naghdi model*, J. Comput. Phys. 229-6 (2010), 2034-2045.
- [20] J. LIU, H. GOMEZ, J.A. EVANS, T.J. HUGHES, C.M. LANDIS, *Functional entropy variables: a new methodology for deriving thermodynamically consistent algorithms for complex fluids, with particular reference to the isothermal Navier-Stokes-Korteweg equations*, J. Comput. Phys. 248 (2013) 47-86.

- [21] R. J. LEVEQUE, *Finite Volume Methods for Hyperbolic Problems*, Cambridge University Press (2002).
- [22] M. MARTIN, S. BOURGEOIS, B. COCHELIN, F. GUINOT, *Planar folding of shallow tape springs: the rod model with flexible cross-section revisited as a regularized Ericksen bar model*, Int. J. Sol. Struct. 188-189 (2020), 189-209.
- [23] E. PICAULT, P. MARONE-HITZ, S. BOURGEOIS, B. COCHELIN, F. GUINOT, *A planar rod model with flexible cross-section for the folding and the dynamic deployment of tape springs: improvements and comparisons with experiments*, Int. J. Solids Struct. 51-18 (2014), 3226-3238.
- [24] E. PICAULT, S. BOURGEOIS, B. COCHELIN, F. GUINOT, *A rod model with thin-walled flexible cross-section: extension to 3D motions and application to 3D foldings of tape springs*, Int. J. Solids Struct. 84 (2016), 64-81.
- [25] C. ROHDE, *Fully Resolved Compressible Two-Phase Flow: Modelling, Analytical and Numerical Issues*, New Trends and Results in Mathematical Description of Fluid Flows (pp. 115-181), Birkhauser (2018).
- [26] K. SEFFEN, S. PELLEGRINO, *Deployment dynamics of tape springs*, Proc. Royal Soc. A 455 (1999), 1003-1048.
- [27] P. SWART, P. J. HOLMES, *Energy minimization and the formation of microstructure in dynamic anti-plane shear*, Arch. Ration. Mech. Anal. 121 (1992), 37-85.
- [28] E. F. TORO, *Riemann Solvers and Numerical Methods for Fluid Dynamics. A Practical Introduction*, Springer-Verlag (1999).
- [29] L. TRUSKINOVSKY, G. ZANZOTTO, *Ericksen's bar revisited: energy wiggles*, J. Mech. Phys. Solids 44 (1996), 1371-1408.
- [30] A. VAINCHTEIN, *Dynamics of phase transitions and hysteresis in a viscoelastic Ericksen's bar on an elastic foundation*, J. Elasticity 57 (1999), 243-280.
- [31] R. VELASCO-SEGURA, P. RENDON, *A finite volume approach for the simulation of non-linear dissipative acoustic wave propagation*, Wave Motion 58 (2015), 180-195.
- [32] S. WALKER, G. AGLIETTI, *A study of tape spring fold curvature for space deployable structures*, Proc. Inst. Mech. Eng. Part G (J. Aerosp. Eng.) 221 (2007), 313-325.